ORIGINAL RESEARCH ARTICLE

Influence of Hot Band Annealing on Cold-Rolled Microstructure and Recrystallization in AA 6016

ELISA CANTERGIANI, IRMGARD WEIßENSTEINER, JAKOB GRASSERBAUER, GEORG FALKINGER, STEFAN POGATSCHER, and FRANZ ROTERS

The influence of an intermediate heat treatment at the end of hot rolling and before cold rolling on Cube texture formation during the final solution annealing of AA 6016 is investigated. Three hot bands with different initial grain sizes and textures are considered: the first one without annealing before cold rolling, while the other two hot bands are heat treated at 540 °C for 1 hour in air before being cold rolled. One of the heat-treated hot bands was left to cool down in air and the other inside the furnace. Electron-backscatter diffraction (EBSD) maps of the cold-rolled specimens and crystal plasticity simulations show no difference in the amount of Cube remaining in the microstructure at the end of cold rolling for all three specimens. The initial grain size of the hot band has no influence on the Cube texture fraction left in the microstructure at the end of cold rolling for thickness reductions higher than 65 pct. Nevertheless, the grain size of the hot band affects the shape and distribution of the Cube grains left in the microstructure and the kernel average misorientation in the cold-rolled specimens. Moreover, the heat treatment decreases the intensity of the beta fiber components (Brass, Copper, and S) in the hot band and promotes the formation of a cold-rolled microstructure with a low kernel average misorientation. Both these factors lower the probability of preferential Cube nucleation during solution annealing and keep the Cube volume fraction after recrystallization below 10 pct, while it reaches 25 pct without intermediate annealing.

https://doi.org/10.1007/s11661-022-06846-4

I. INTRODUCTION

OPTIMIZATION and tailoring of texture is fundamental to reduce anisotropy of aluminum sheets during forming, especially in 6xxx alloys because of their use in automotive components, where surface finish and shape must satisfy strict requirements. Alloys of 6xxx series are of interest in automotive applications because of their good combination of formability, corrosion resistance, and increase of strength during paint baking after forming.[1] Texture evolution depends on casting,[2] hot and cold rolling parameters (strain rate[3] and temperature), deformation history,[4–6] alloy composition,[7] and the presence of precipitates.[8,9] After cold rolling, the 6xxx sheets are solution annealed (SA) at a temperature between 500 °C and 570 °C followed by quenching to dissolve the hardening phases and retain the corresponding alloying elements in solid solution.[1,4] During this solution treatment, recrystallization of the cold-rolled sheet occurs resulting in a modified texture. Cube is considered a critical texture component during the recrystallization treatment because it can show preferential nucleation and growth.[10] Cube preferential growth during recrystallization is found mostly in high-purity aluminum alloys[11]; however, also 6xxx alloys stabilize a high fraction of Cube during hot rolling which can be difficult to remove during successive cold rolling.[11,12] This fraction of Cube left in 6xxx alloys can show preferential nucleation during the final solution annealing. Recrystallized Cube grains can originate from transition bands,[13] which are thin Cube seeds surrounded by high orientation gradients and that are caused by diverging rotations of unstable orientations according to the Dillamore and Katoh model.[14,15] However, also Cube fragments left in the microstructure at the end of cold rolling and not exactly corresponding to transition bands can act as nucleation sites.[16,17] During *in situ* annealing experiments and modeling of commercial AlFeSi alloy, Sukhopar and Gottstein[18]

ELISA CANTERGIANI and FRANZ ROTERS are with the Max-Planck-Institut für Eisenforschung, Max-Planck-Straße 1, 40237 Düsseldorf, Germany. Contact e-mail: e.cantergiani@mpie.de IRMGARD WEIßENSTEINER and STEFAN POGATSCHER are with the Christian Doppler Laboratory for Advanced Aluminum Alloys, Montanuniversitaet Leoben, 8700 Leoben, Austria. Contact e-mail: irmgard.weissensteiner@unileoben.ac.at JAKOB GRASSERBAUER is with the HTL Leoben, Max-Tendler-Strasse 3, 8700 Leoben, Austria. GEORG FALKINGER is with the AMAG Rolling GmbH, 5282 Ranshofen, Austria.
Manuscript submitted July 25, 2022; accepted September 29, 2022.
Article published online October 30, 2022

have shown that the intensity of Cube texture after recrystallization is due to nucleation at the Cube bands left in the deformed microstructure, while contribution to Cube nucleation from locations outside the Cube bands is negligible. Recrystallization in high purity and highly deformed (98 pct cold rolled) aluminum foil has shown that occurrence of extensive recovery and continuous recrystallization can retard the formation of Cube texture.[19]

The recrystallization advantage of Cube grains decreases rapidly when the Cube present in the microstructure is misoriented at least 10 to 15 deg from its exact orientation.[20] Thus, several works were dedicated to increasing the Cube fragmentation during rolling through asymmetric cold rolling[4] or with the adjustment of shear loading.[21,22] Some experimental investigations have suggested that a fraction of Cube texture could be created by S-oriented grains during compression,[23] while elasto-viscoplastic fast Fourier transform (EVP-FFT) simulations have shown that depending on the amount of compression strain, some Cube can originate from random orientations or non-Cube grains misoriented within 10 to 20 deg from ideal Cube,[24] but the fraction of this newly formed Cube during rolling is extremely low and it does not play a key role during recrystallization.

Solutions to reduce the amount of Cube already during casting were suggested through the use of continuous casting (CC) instead of direct casting (DC). For the same aluminum alloy, CC produces ND misoriented Cube microstructures, while DC forms microstructures containing a higher fraction of perfectly oriented Cube.[2] During cold rolling, Brass, Copper, and S develop faster in hot bands from CC than DC; moreover, microstructures from DC maintain a higher fraction of exact Cube orientation at the end of cold rolling.[25] In several aluminum alloys, the amount of Brass texture was increased and the Cube fraction was lowered by tailoring the alloy composition.[7,26,27]

Cube recrystallization has been the object of several investigations at microtexture level using bicrystal plane strain compression tests.[28,29] Initially, the attention was focused on the role of grain boundaries and Cube transition bands in the nucleation of new grains. In particular, subgrain coalescence in transition bands helps Cube nuclei in reaching early the critical size to grow.[30] More recently, the influence of different amounts of iron content, deformation strain, and recrystallization temperature on Cube texture in AA 1145 has been presented.[31] The recrystallized texture depends on a competition between Cube, R orientation, and particle stimulated nucleation (PSN). Preferred Cube nucleation is obtained at low strain and low recrystallization temperature because the fast Cube recovery prevails over recrystallization of other texture components; while R-oriented grains nucleate preferably at grain boundaries whose density is favored by high strain deformations.[31]

Another microstructure heterogeneity that influences Cube recrystallization is represented by shear bands. In Al–Mg alloys, shear bands possess high-angle grain boundaries that can already migrate at low temperatures (200 °C to 350 °C) and favor the nucleation of new grains.[32] At these temperatures, the nucleation at shear bands is found to be more rapid than formation of nuclei at other microstructure heterogeneities.[32]

Cube recrystallization has been found to be affected by the presence of concurrent precipitation in supersaturated aluminum alloys.[33] In Al–*x*Mn–Fe–Si alloys, concurrent precipitation enhances the presence of P and ND rotated Cube grains, while it suppresses or retards nucleation and growth of exactly oriented Cube.[33] These results were confirmed by Tangen *et al.*[34] who investigated the influence of concurrent precipitation during recrystallization in a manganese supersaturated aluminum alloy. Tangen *et al.*[34] concluded that concurrent precipitation leads to an inhomogeneous coarse-grained microstructure which is dominated by P and ND rotated Cube orientations.

The influence of different textures and microtexture for the same alloy system (AA 1050) on Cube recrystallization was investigated by comparing Cube nucleation and growth of plane strained compressed (PSC) microstructure and equal channel angular extruded (ECAE) microstructures.[35,36] Despite the fraction of Cube grains was the same after both deformation routes, a higher intensity of Cube texture was found after recrystallization in plane strain compressed microstructures because of the presence of strong S texture.[35] Recrystallization of microstructures from ECAE deformation did not show Cube growth because of the absence of S orientation in the deformed microstructure.[35] Recently, the influence of pressure on recrystallization of AA 3003 alloy was investigated proving that the presence of pressure during the thermal treatment can refine the recrystallized grains, weaken the pinning effect, and strengthen P and ND rotated Cube.[37]

The purpose of this work is to present a solution to limit Cube recrystallization in AA 6016 by introducing an intermediate annealing at the end of hot rolling and before cold rolling. The aim is to investigate how this intermediate annealing changes the microstructure (grain size and texture) during cold rolling and final solution annealing. It is important to assess if there is an influence of hot band grain size and texture on Cube texture evolution in AA 6016 during cold rolling and to experimentally see how the cold-rolled microstructures obtained from different hot bands change after the final solution annealing. Microstructures right after industrial cold rolling are compared with textures from full-field crystal plasticity simulations. This simulation approach allows to investigate the influence of initial hot

Table I. Chemical Composition of Alloy AA 6016 in Wt Pct

Alloy	Mg	Mn	Fe	Si	Al
EN AW-6016	0.35	0.07	0.19	1.14	bal.

band texture and grain size on Cube texture evolution during cold rolling. Analysis of distribution and fragmentation of Cube orientation is performed both on experiments and simulations.

II. EXPERIMENTAL AND COMPUTATIONAL METHODS

A. *Experimental Methods*

The aluminum AA 6016 used for the hot bands had the composition is shown in Table I. Starting from this cast material, three hot bands were prepared on the hot rolling plant at Austria Metall AG (AMAG) rolling GmbH. After hot rolling, one coil was used for cold rolling in the industrial plant at AMAG, while the other two coils were subjected to intermediate annealing at 540 °C for 1 hour before undergoing the same cold rolling schedule. Thus, for cold rolling, three hot bands were available:

- Hot band A: without intermediate annealing between hot and cold rolling;
- Hot band B: with intermediate annealing at 540 °C for 1 hour with cooling in air;
- Hot band C: with intermediate annealing at 540 °C for 1 hour with cooling inside the furnace.

RD–ND sections from the three hot bands were prepared by grinding, mechanical polishing with diamond suspensions and oxide polishing suspension (OPS, Struers) with contact forces up to 50 N for at least 18 min. This final polishing was followed by electrochemical polishing using STRUERS A2 electrolyte at 10 °C for 4 to 8 seconds and a voltage of 36 V. This procedure has been already used by the authors for the preparation of several AA 6016 specimens.[38] Electron-backscatter diffraction (EBSD) analyses were performed using a scanning electron microscope (SEM; JEOL 7200F FEG-SEM, Tokyo, Japan) equipped with an EBSD-measurement system (Nordlys Nano and Symmetry S2, Oxford Instruments, Abingdon, UK) with a 70 deg tilt specimen at 20 kV. For hot band A, the EBSD scans covered the whole sheet thickness (area of 2000 μm $\times$ 7000 μm with step size of 3 μm). For hot bands B and C, three measurements each of size 820 μm $\times$ 7000 μm with a step size of 4 μm were performed for each sample to obtain a sufficient amount of grains orientations to evaluate texture due to the larger grain size in hot band B and C.

All hot bands with an initial thickness of 7.0 mm were cold rolled down to 1.3 mm (corresponding to a total thickness reduction of $\approx$ 82 pct). Cold rolling was performed on the industrial plant at AMAG rolling GmbH.

EBSD analyses were performed on RD–ND sections of the cold-rolled specimens to evaluate the Cube texture distribution through thickness and the texture evolution obtained from the three hot bands. Cold-rolled samples for EBSD were prepared through standard grinding with 1000 and 2000 SiC papers before proceeding with 3 μm polishing with diamond suspension. The final polishing was done manually for approximately 1 hour with OPS suspension (Struers) with the addition of 10 pct of hydrogen peroxide (H_2O_2). EBSD maps were obtained using a field emission SEM-JEOL 6500 F operated at a voltage of 20 kV. For each cold-rolled sample, at least three EBSD scans of the full sheet thickness were obtained using a step size of 1.5 μm.

The cold-rolled samples from different hot bands were then solution annealed (SA) in a salt bath for 5 min at a temperature of 520 °C followed by water quenching. Fully recrystallized microstructures were obtained in each specimen, and EBSD analyses were performed on two areas of at least 1500 μm $\times$ 800 μm with step size of 3 μm for each sample.

For texture evaluation, unless otherwise stated, orientation distribution functions (ODFs) were calculated using MTEX version 5.2.3 and De la Vallee Poussin kernel with a half-width of 5 deg.

B. *Computational Methods*

Crystal plasticity simulations were performed to track the influence of initial grain shape of the hot band on Cube texture evolution. For the three hot bands, high-resolution EBSD scans were performed at the center of the aluminum sheet. The microstructure obtained from these EBSD scans was used to generate starting 2D-RVEs to be used for crystal plasticity simulations with the freeware software package DAMASK.[39] The input files were created by writing a pipeline in DREAM.3D software.[40] A first simulation compared an RVE from hot band A with an RVE from hot band B with the same initial Cube fraction. Another simulation was performed on an RVE from hot band A and RVE from hot band C again with the same initial Cube volume fraction. The RVEs were then deformed in plane strain compression applying the compression history given in Table II, while the component of the deformation gradient $F_{\text{TD–TD}}$ is equal to 1.0 and the other components $F_{\text{RD–TD}}$, $F_{\text{RD–ND}}$, $F_{\text{TD–ND}}$ are all set to zero. During deformation of the polycrystalline RVE,

Table II. Number of Rolling Passes Simulated in DAMASK for Cold Rolling of AA 6016 with the F_{ND-ND} Value Implemented in the Simulation and the Corresponding Thickness Reduction

Rolling Pass	F_{ND-ND}	Thickness Reduction Per Pass (Pct)	Total Thickness Reduction (Pct)
1st	0.67	33	33
2nd	0.82	18	45
3rd	0.82	18	55
4th	0.87	13	60.8
5th	0.87	13	65.9
6th	0.85	15	71
7th	0.85	15	75.4
8th	0.87	13	78.6
9th	0.87	13	81.4

the initial grid of material points becomes distorted because of deformation heterogeneity in each grain. When the distortion becomes too large, the stress equilibrium cannot be found, and convergence is not reached. Thus, to simulate compression higher than 40 to 50 pct of thickness reduction, a remeshing scheme is implemented in DAMASK. During remeshing, a new undistorted grid is created and the state variables from the previous deformation step are mapped onto the newly created grid using a nearest-neighbor mapping algorithm. The next cold rolling step is then performed with the new undistorted grid. During remeshing, the elastic deformation is relaxed. A detailed description of the implemented remeshing scheme is described by Sedighiani *et al.*[41] and its influence on texture prediction was already assessed, showing that the number of remeshing step does not affect texture evolution.[3]

1. *Constitutive model for crystal plasticity simulations*

The plastic deformation is described through the plastic deformation gradient ($\boldsymbol{F}_p$) whose evolution is given as:

$$\dot{\boldsymbol{F}}_p = \boldsymbol{L}_p \boldsymbol{F}_p. \quad [1]$$

In Eq. [1], the plastic velocity gradient ($\boldsymbol{L}_p$) can be formulated as sum of the shear rates on all slip systems as:

$$\boldsymbol{L}_p = \boldsymbol{E}_p \boldsymbol{F}_p^{-1} = \sum_{\alpha=1}^{n} \dot{\gamma}^{\alpha} \boldsymbol{m}^{\alpha} \otimes \boldsymbol{n}^{\alpha}, \quad [2]$$

where $\boldsymbol{m}^{\alpha}$ represents the slip direction and $\boldsymbol{n}^{\alpha}$ is the normal to the slip plane of slip system α, while $\dot{\gamma}^{\alpha}$ is the shear rate of the αth slip system and n is the number of slip systems. For cold rolling simulations, the 12 octahedral slip systems (*i.e.*, $\{111\}\ \langle 110 \rangle$) are considered in the calculation of the plastic velocity gradient.

Table III. Parameters of the Pheno-power Law Used in DAMASK for Cold Rolling Simulations

Parameter	Value
C_{11}	106.75 GPa
C_{12}	60.41 GPa
C_{44}	28.34 GPa
$\dot{\gamma}_0$	0.001 s^{-1}
$1/m$	20
τ_c^{β}	31 MPa
τ_s	63 MPa
a	2.25
h_0	75 MPa
$q_{\alpha\beta}$ (Self and Coplanar Slip Systems)	1.0
$q_{\alpha\beta}$ (Non-coplanar Slip Systems)	1.4

For the shear rate, the constitutive behavior of aluminum was described by a pheno-power law, whose parameters are listed in Table III and whose description has already been used for aluminum texture simulations and prediction.[3,42] In Table III, C_{11}, C_{12}, and C_{44} are the elastic constants, $\dot{\gamma}_0$ is the reference shear strain rate, m is the strain rate sensitivity exponent, τ_c^{β} is the critical shear stress for slip system β, and τ_s, a, and h_0, represent the saturation value of slip resistance, the hardening exponent, and the initial hardening coefficient, respectively. The latent hardening ($q_{\alpha\beta}$) is set to 1.0 for coplanar slip systems and 1.4 for non-coplanar slip systems to make the hardening model anisotropic. In phenomenological constitutive models, the shear rate on slip system α is a function of the critical resolved shear stress (τ_c^{α}) and the resolved shear stress for slip system α (τ^{α}) according to:

$$\dot{\gamma}^{\alpha} = \dot{\gamma}_0 \left| \frac{\tau^{\alpha}}{\tau_c^{\alpha}} \right|^{1/m} \mathrm{sign}(\tau^{\alpha}), \quad [3]$$

where $\dot{\gamma}_0$ is the reference shear strain rate and m is the strain rate sensitivity exponent. The evolution of the critical resolved shear stress is expressed as:

$$\dot{\tau}_c^{\alpha} = \sum_{\beta=1}^{n} h_{\alpha\beta} \left| \dot{\gamma}^{\beta} \right|, \quad [4]$$

This equation describes the influence of any set of slip system (β) on the hardening behavior of a (specific) slip system α through the hardening matrix ($h_{\alpha\beta}$). This hardening matrix captures the micromechanical interaction among different slip systems and it is given by:

$$h_{\alpha\beta} = q_{\alpha\beta} \left[h_0 \left(1 - \frac{\tau_c^{\beta}}{\tau_s} \right)^{a} \right] \quad [5]$$

with h_0, a, and τ_s representing the self-hardening coefficient, the hardening exponent, and the saturation value of slip resistance, respectively. These parameters are

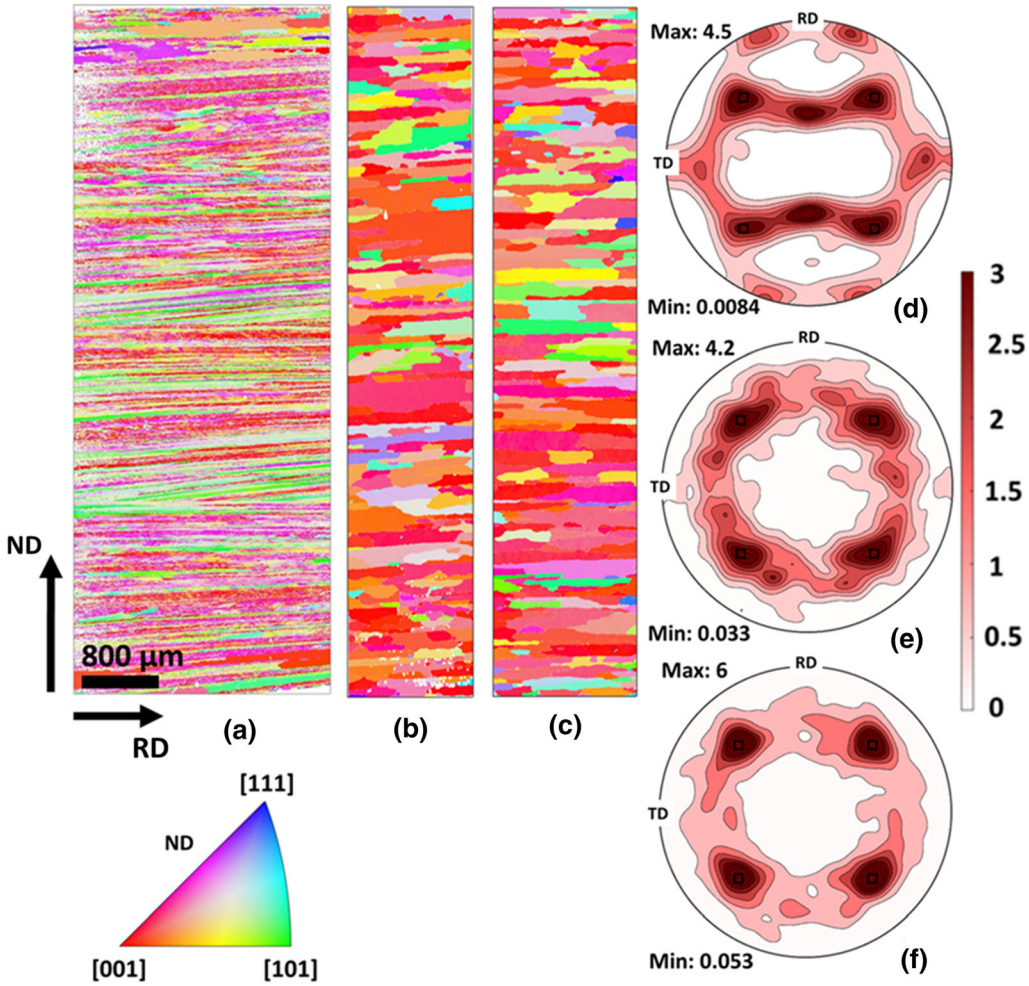

Fig. 1—IPF for normal direction (ND) of the RD–ND section for (*a*) hot band without annealing, (*b*) and (*c*) hot bands after annealing at 540 °C for 1 h and subsequent air and furnace cooling, respectively. (111) Pole figures for hot bands without annealing (*d*) and for hot bands with annealing and air cooling (*e*) or furnace cooling (*f*).

assumed to be identical for all FCC slip systems. The parameter $q_{\alpha\beta}$ is calculated as:

$$q_{\alpha\beta} = \left(q_{\text{lat}} + (q_{\text{self}} - q_{\text{lat}})\delta_{\alpha\beta}\right), \quad [6]$$

where $\delta_{\alpha\beta}$ is the Kronecker delta and q_{self} and q_{lat} are the self and latent hardening, respectively. The hardening matrix contains diagonal terms (q_{self}) and off-diagonal terms (q_{lat}). The latent hardening is set to 1.0 for coplanar slip systems and 1.4 for non-coplanar slip systems to make the hardening model anisotropic.

III. RESULTS AND DISCUSSION

A. *Hot Rolling Microstructure and Texture*

Figure 1 shows RD–ND microstructures for the three hot bands with the corresponding ODF as (111) pole figures. The pole figure plots in Figure 1 for hot bands B and C are obtained by considering all EBSD maps from the three RD–ND sections, so that the analyzed volume is comparable to the sample from hot band A. The other EBSD maps for hot bands B and C are available in "Appendix" (Figure A-I).

The hot band without heat treatment has thin grains elongated along RD, while the annealed hot bands show large grains. From the (111) pole figures, hot band A has a high density of Cube texture with a fully developed beta fiber (Figure 1(d)), while hot bands B (Figure 1(e)) and C (Figure 1(f)) show a high intensity for Cube texture or random orientations, but the beta fiber is suppressed because of the annealing.

Figure 2 shows the distribution of Cube grains through the whole thickness for the three hot bands and Figure 3 shows the volume fractions calculated considering up to 15 deg maximum misorientation of the relevant orientations listed in Table IV for the three hot bands. In Figure 3, the amount of Brass, Copper,

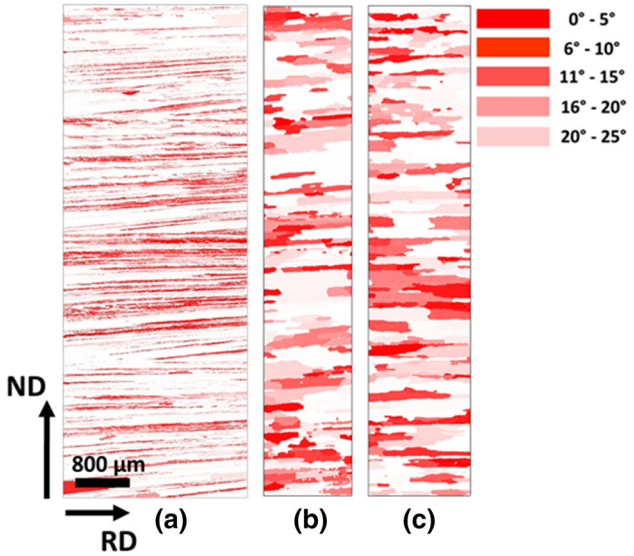

Fig. 2—Cube maps on the RD-ND section for: hot band without annealing (hot band A) (*a*), hot band after annealing at 540 °C for 1 h with cooling in air (hot bands B) (*b*), and hot band after annealing at 540 °C for 1 h with cooling inside the furnace (hot bands C) (*c*).

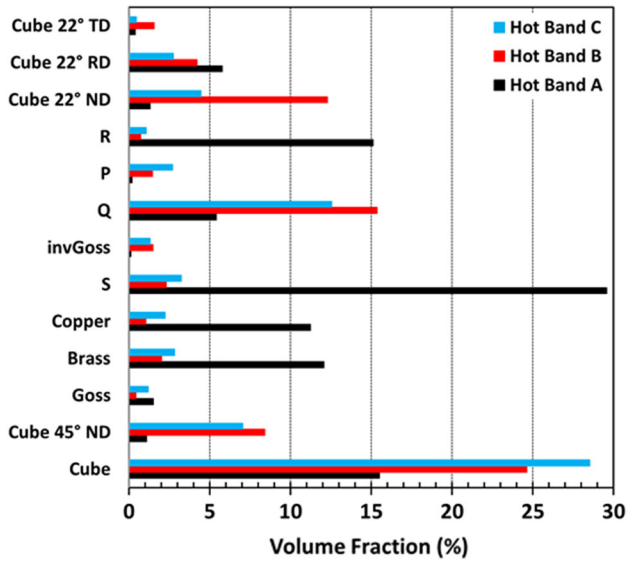

Fig. 3—Volume fraction of several texture components for the three different hot bands.

and S are low in hot bands B and C confirming that the β fiber components have been attenuated by the annealing.

Annealed hot band textures are dominated by Cube, Q and 45 deg ND rotated Cube, while the fractions of beta fiber orientations (Brass, Copper, and S) and R are low, indicating that during annealing before cold rolling, the recrystallization inside the hot-rolled specimen is driven by nucleation at cube bands and shear bands. The contribution of Cube transition bands, strain-induced boundary migration, shear bands, and PSN on texture development during annealing and recrystallization has been investigated by Lücke and Engler[8] and Engler.[43] It was concluded that Cube emerges from nuclei at transition bands that show preferential growth into S and rolling texture components (like Copper), while formation of 45 deg ND rotated Cube and Q orientations is caused by nucleation at shear bands (preferentially shear bands pertaining to S orientations).[43]

B. *Cold Rolling Microstructure and Texture*

Figure 4 shows one RD–ND scan and the corresponding Cube distribution map for the cold-rolled samples from each hot band. The other EBSD maps obtained from cold-rolled specimens are included in "Appendix" (Figure A-II). In Figure 4, the volume fraction of Cube is comparable for all cold-rolled samples and this suggests that the Cube grain shape and size initially present in the hot bands have no influence on the fraction of Cube texture. However, the Cube morphology and distribution appear different. The cold-rolled sample from hot band A has thin Cube seeds distributed almost through the whole thickness (Figure 4(b)), while samples from hot bands B and C show thick Cube bands only in some zones across the thickness of the sample (Figures 4(d) and (f)). A similar impact of the hot band grain size on the Cube shape and distribution left in the microstructure at the end of cold rolling was described by Engler.[44] Fine grained hot bands yield to a large number of Cube transition bands parallel to the rolling direction. These transition bands are favorable interfaces for Cube nucleation and, in fine grained samples, they are narrow spaced in the RD–ND section making the Cube nucleation and growth more efficient than PSN or nucleation on shear bands.[44,45] Contrary, in samples from coarse-grained hot bands, few Cube interfaces are present in the RD–ND sections and even after heavy deformation the grains remain thick in the microstructure. As a consequence, Cube bands are too far apart and have too few interfaces to produce many nuclei, and for these coarse microstructures, PSN will be the predominant recrystallization mechanism.[44]

Figure 5 shows the fraction of relevant texture components found on each EBSD map (in Figure 4 and in "Appendix", Figure A-II) for the cold-rolled samples obtained from the different hot bands. The volume fraction of Cube ranges from 1.5 to 5 pct for all samples suggesting that the larger grain shape in the hot band does not promote more Cube fragmentation during cold rolling than elongated thin grains, but it influences the shape of the remnant Cube grains inside the microstructure. A higher fraction of Brass and S is found for specimens cold rolled from hot band A, while cold-rolled sheets from the annealed hot bands (B and C) exhibit higher fraction of Copper. A higher fraction of Copper at the expenses of S orientation was also found in overaged Al–1.8 pct Cu alloys rolled from hot bands with coarse grain size.[44] The development of rolling texture (*i.e.*, β fiber components) is retarded in coarse-grained materials because a higher level of deformation heterogeneities can occur in such microstructures including deformation bands, shear bands and splitting of

Table IV. Crystallographic Orientations Considered to Quantify the Evolution of Aluminum Texture from Different Hot Bands

Crystallographic Orientation	$\{hkl\}$ ||ND + $\langle uvw \rangle$|| RD	Euler Angles (φ_1, Φ, φ_2) (Deg)
Cube	$\{001\}\langle 100\rangle$	(0, 0, 0)
Rotated Cube 45 Deg ND	$\{001\}\langle 110\rangle$	(45, 0, 0)
Brass	$\{110\}\langle 112\rangle$	(35, 45, 0)
S	$\{123\}\langle 634\rangle$	(59, 34, 65)
Copper	$\{112\}\langle 111\rangle$	(90, 35, 45)
Goss	$\{011\}\langle 100\rangle$	(0, 45, 0)
Q	$\{013\}\langle 231\rangle$	(45, 15, 10)
P	$\{011\}\langle 122\rangle$	(70, 45, 0)
R	$\{124\}\langle 211\rangle$	(63, 31, 60)
invGoss	$\{0-11\}\langle 011\rangle$	(90, 45, 0)
Rotated Cube 22 Deg ND	$\{001\}\langle 5-20\rangle$	(22, 0, 0)
Rotated Cube 22 Deg RD	$\{025\}\langle -100\rangle$	(0, 22, 0)
Rotated Cube 22 Deg TD	$\{025\}\langle 0-52\rangle$	(90, 22, 0)

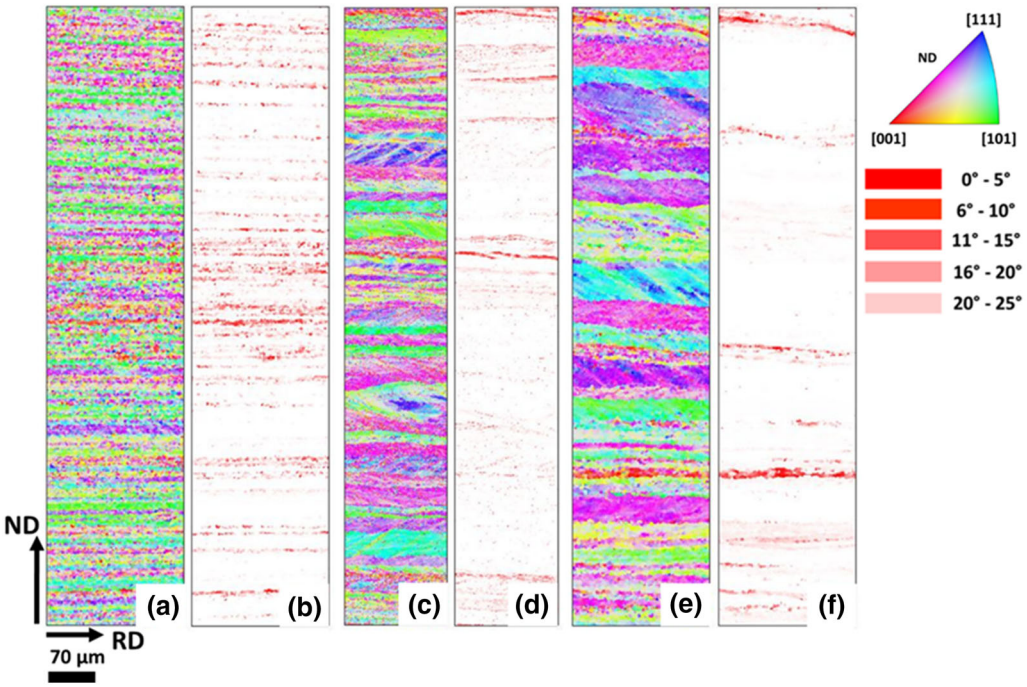

Fig. 4—IPF for normal direction (ND) of the RD–ND section for cold-rolled samples from hot band A (*a*), hot band B (*c*), and hot band C (*e*). Cube distribution through thickness for cold-rolled samples from hot band A (*b*), from hot band B (*d*), and from hot band C (*f*).

orientations which retard the development of a sharp texture.[44,46]

C. *Solution Annealing Microstructure and Texture*

Figure 6 shows one RD–ND section of an EBSD scan for each specimen and the corresponding map of the Cube grain distribution for SA samples. Further EBSD maps used to evaluate texture volume fractions are included in "Appendix" (Figure A-III). The Cube distribution maps show more grains pertaining to the exact Cube orientation in the sample from hot band A. However, no preferential growth of Cube occurred as the grain size is the same in all samples, but the higher fraction of Cube in the sample from hot band A seems to be caused by preferential nucleation. Preferential Cube growth with Cube grains much coarser than grains pertaining to other orientations is often found in high-purity aluminum and the strength of Cube texture is known to decrease with alloy content.[47]

The recrystallized microstructures in Figure 6 all show similar grain sizes. According to literature,[44] this

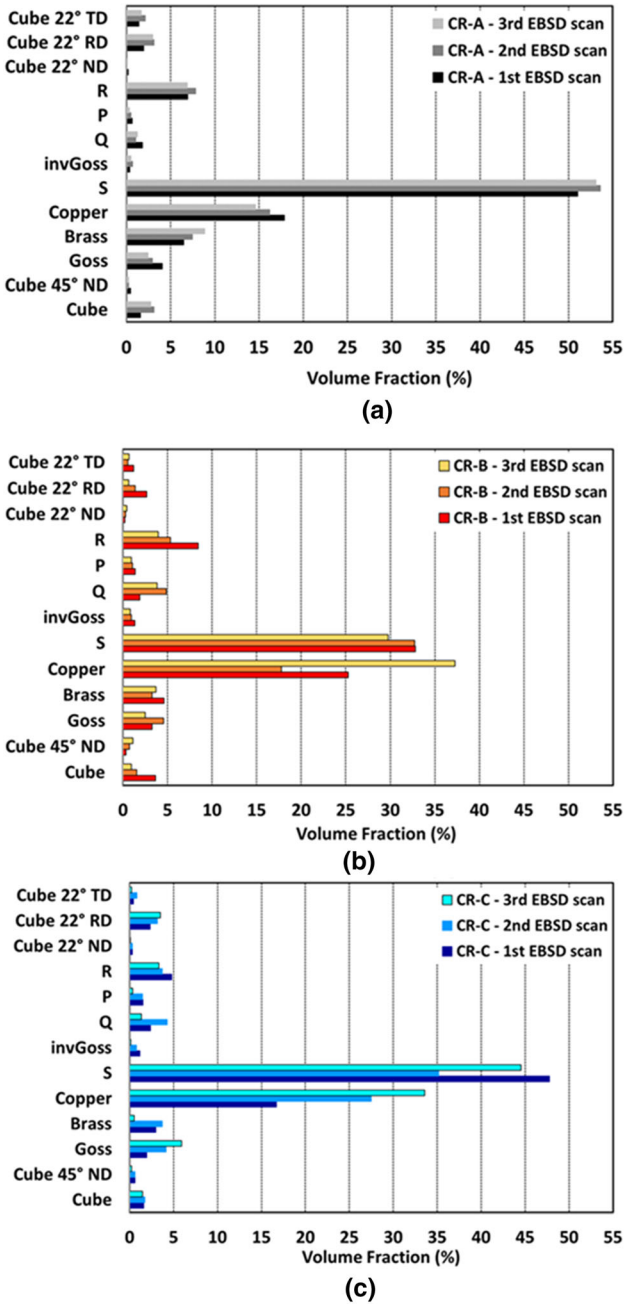

Fig. 5—Volume fraction of texture components calculated from EBSD scans of the whole sheet thickness for cold-rolled samples obtained from hot band A (CR-A) (*a*), for cold-rolled samples obtained from hot band B (CR-B) (*b*), and for cold-rolled samples obtained from hot band C (CR-C) (*c*).

is an indication of texture being determined by the superposition of recrystallization occurring at various nucleation sites (Cube bands, shear bands, and PSN). Figure 7 presents the volume fraction of texture components after solution annealing. The cold-rolled sample from hot band A shows the highest Cube fraction among all samples and also preserves a high fraction of S orientation. Samples from hot bands B and C have 8 to 9 pct of Cube fraction, and the volume fractions of the β fiber components (Brass, Copper and S) do not overcome 5 pct. In Figure 7, the higher Cube and S fractions in the sample from hot band A can be caused by a higher fraction of S orientation and β fiber present in the cold-rolled specimen. Cube shows preferential nucleation when surrounded by S orientation.[43] R orientation prevails in the microstructures from hot band A and it can be generated by strain-induced boundary migration (SIBM) but also it is preferentially nucleated in microstructures with high fractions of S texture because of a 40 deg ⟨111⟩ relation with S.[43] Moreover, R is assumed to easily nucleate at grain boundaries.[44] Samples from hot bands B and C have higher fraction of Q and P orientations than the specimen from hot band A. Predominance of P and 45 deg ND rotated Cube in samples from hot bands B and C can be a consequence of PSN.[43,44] However, it was also shown that strong P and Q components can occur at the expenses of Cube when nucleation at shear bands is predominant.[44,48] Microstructure from hot band A has a higher fraction of 22 deg RD rotated Cube which can be attributed to nucleation at Cube transition bands,[44] while 22 deg TD rotated Cube fraction is higher in microstructures from hot bands B and C. This higher fraction of 22 deg TD rotated Cube could be a result of PSN. In AA 3104 alloys, EBSD data have shown that dispersoids with major size lower than 0.6 μm do not affect texture evolution, while significant orientation gradients are found around coarse particles. These orientation gradients are characterized by lattice rotations in TD direction.[49]

D. *Crystal Plasticity Simulations Results*

For crystal plasticity simulations, two zones were extracted as input from hot band A. The first zone named hot band A (1) which has the same amount of Cube fraction as the initial input microstructure from hot band B. The second zone named hot band A (2) which has the same amount of Cube fraction as the initial input microstructure from hot band C.

Figure 8 shows the initial microstructure hot band A (1) and the microstructure from hot band B. Another set of simulations was done taking an initial microstructure hot band A (2) and a microstructure from hot band C (Figure 9), and the evolution of Cube volume fraction was extracted from crystal plasticity simulations. Both Figures 8 and 9 indicate that at 80 pct thickness reduction, the amount of Cube remaining in the microstructure is negligible or even absent according to the simulations.

The evolution of Cube fraction as function of thickness reduction is shown in Figure 10. For a thickness reduction higher than 70 to 80 pct, the Cube

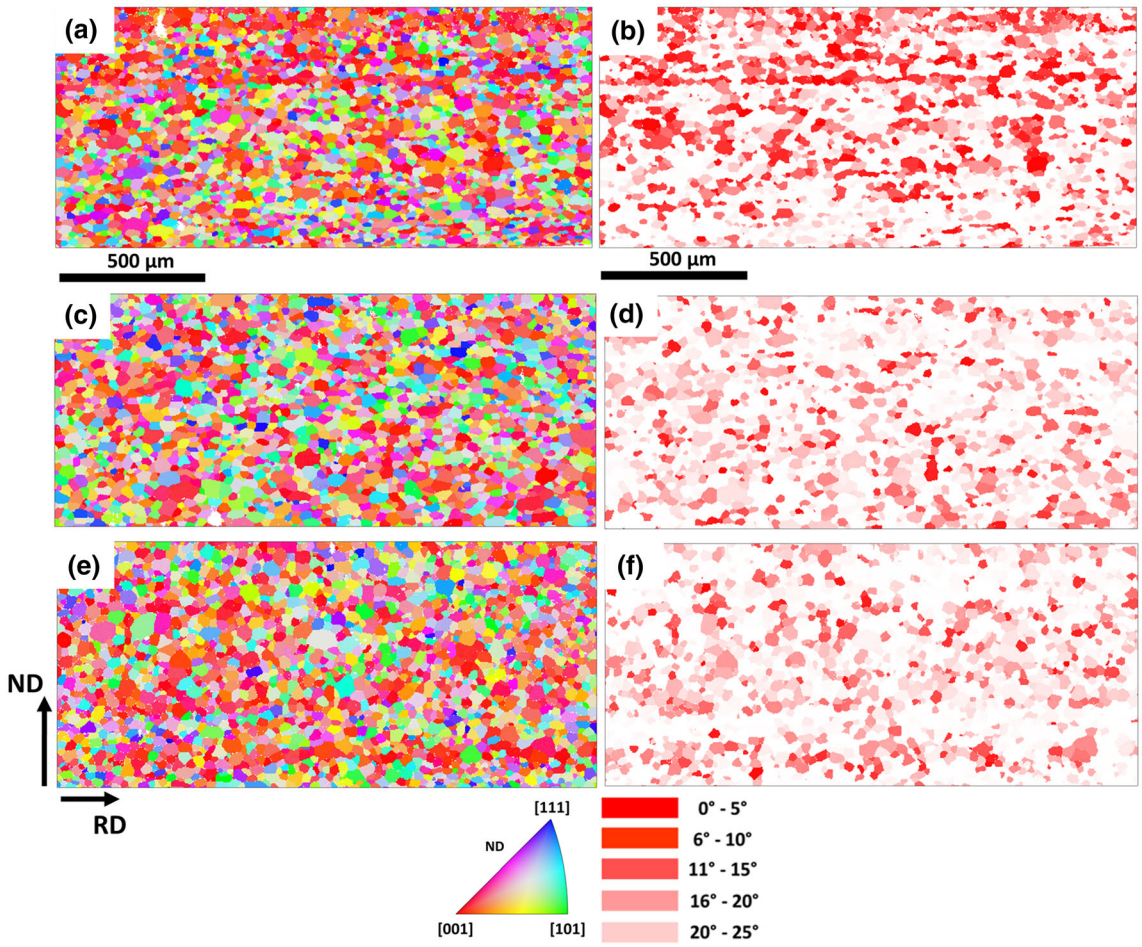

Fig. 6—IPF for normal direction (ND) and distribution of Cube grains after solution annealing (SA) for cold-rolled specimen from hot band A (*a* and *b*), for cold-rolled specimen from hot band B (*c* and *d*), and for cold-rolled specimen from hot band C (*e* and *f*).

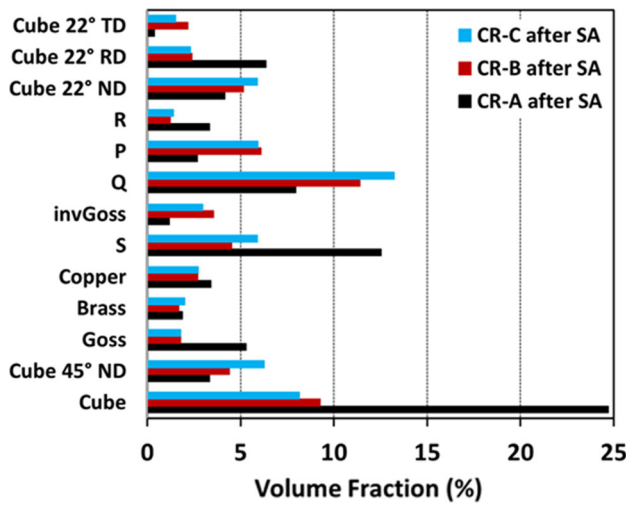

Fig. 7—Volume fraction of texture components calculated from EBSD scans of the whole sheet thickness for cold-rolled (CR) samples obtained from different hot bands (A, B, and C) after solution annealing (SA).

fraction does not depend on the initial grain size of the hot band. Moreover, as shown in Figure 10(b), it can also occur that a higher fraction is predicted for the large grain microstructure than for the elongated grains microstructure. This simulation result confirms the experimental fractions shown in Figure 5 where the Cube fraction varied in the same range for all cold-rolled samples. Moreover, in Figure 10(a), for compressions lower than 50 pct, elongated grains show higher Cube fraction than large grains, the opposite holds in Figure 10(b). Thus, no conclusion can be drawn on the effect of initial grain size of hot bands on Cube fraction evolution during cold rolling. A crystal plasticity simulation was repeated by using a 3D RVE with the same initial texture and amount of Cube, but one RVE had elongated grains and the other had equiaxed grains and no difference could be found in Cube fraction evolution for thicknesses equal or higher than 50 pct. Looking at the experimental Cube volume fractions and at the crystal plasticity simulations results, there is no difference in the amount of Cube remaining after cold

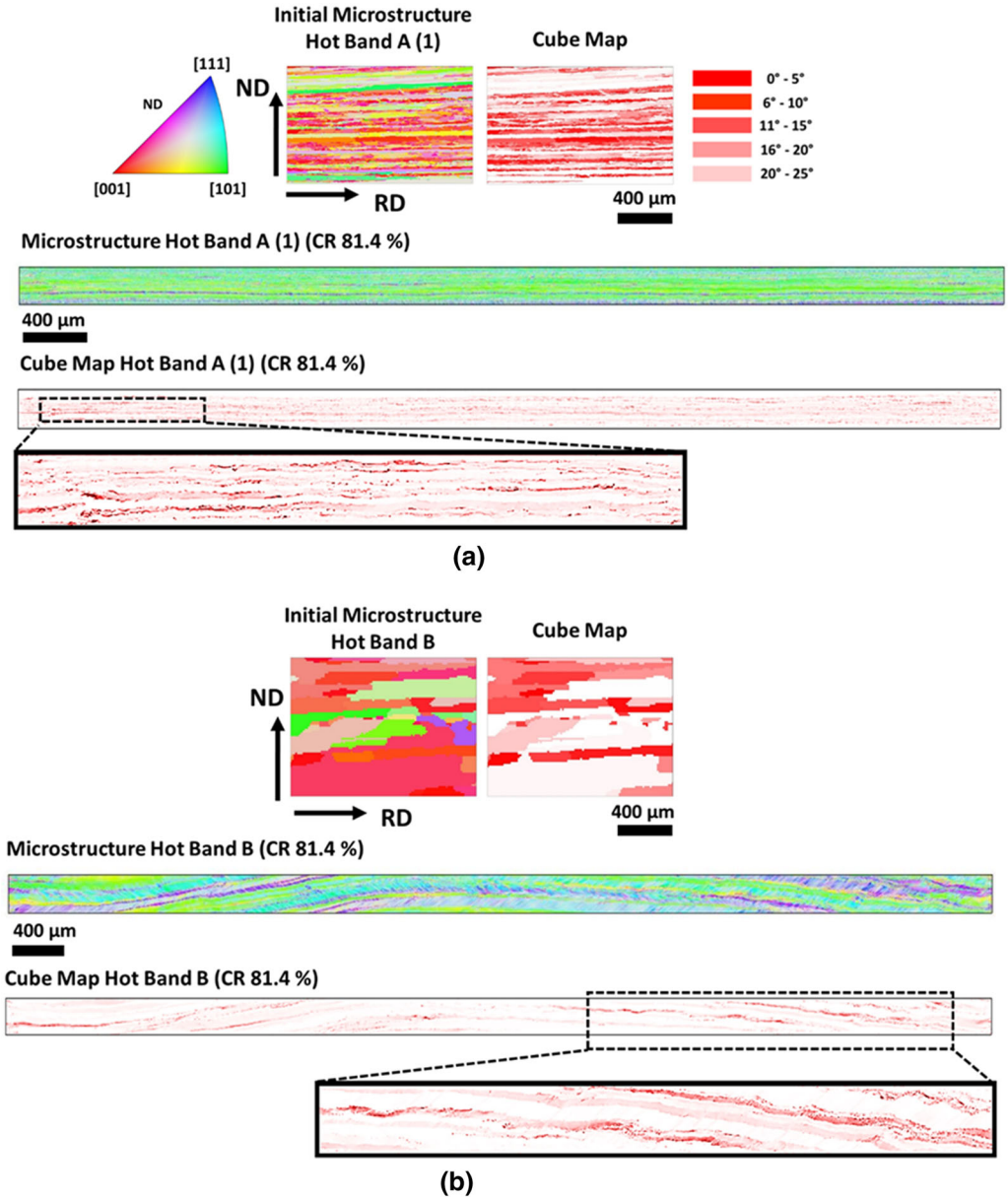

Fig. 8—Initial microstructure and microstructure after 81.4 pct of cold rolling (CR) with corresponding Cube maps obtained from crystal plasticity simulations for hot band A (*a*) and hot band B (*b*).

rolling that could explain why, after solution annealing, there is a lower Cube volume fraction in samples from hot bands B and C.

The prediction of texture from crystal plasticity simulations was compared with the texture obtained experimentally from cold rolling. The ODFs from experiments were obtained from the full thickness RD–ND EBSD maps, and ODFs were calculated with harmonic series expansion with a half-width of 5 deg. Figure 11 shows the comparison between simulations and cold rolling for specimens from hot band A. The Cube intensity is low in both experiments and simulations, while the intensity is at the maximum for the β fiber components (Brass (Br), Copper (Cu), and S). The same result occurs for microstructures cold rolled from hot bands B and C where β fiber texture components have the highest intensity (Figures 12(a) and (c)). In simulations, there is a tendency to overestimate Goss and underestimate Brass when 2D representative volume elements (RVEs) are used to simulate texture evolution. For a 2D RVE, the component of the deformation gradient F_{RD-TD} is zero globally and also

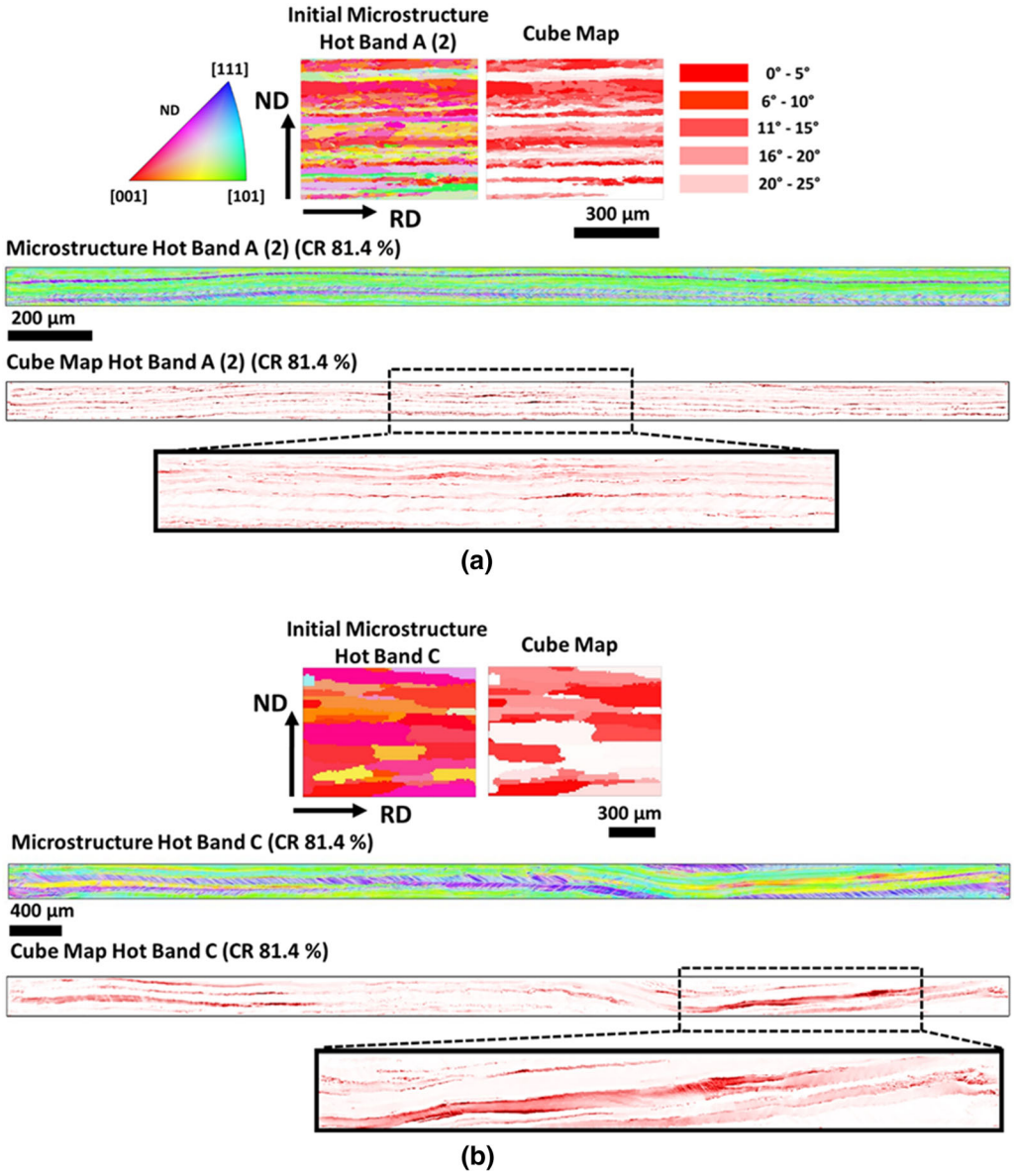

Fig. 9—Initial microstructure and microstructure after 81.4 pct of cold rolling (CR) with corresponding Cube maps obtained from crystal plasticity simulations for hot band A (*a*) and hot band C (*b*).

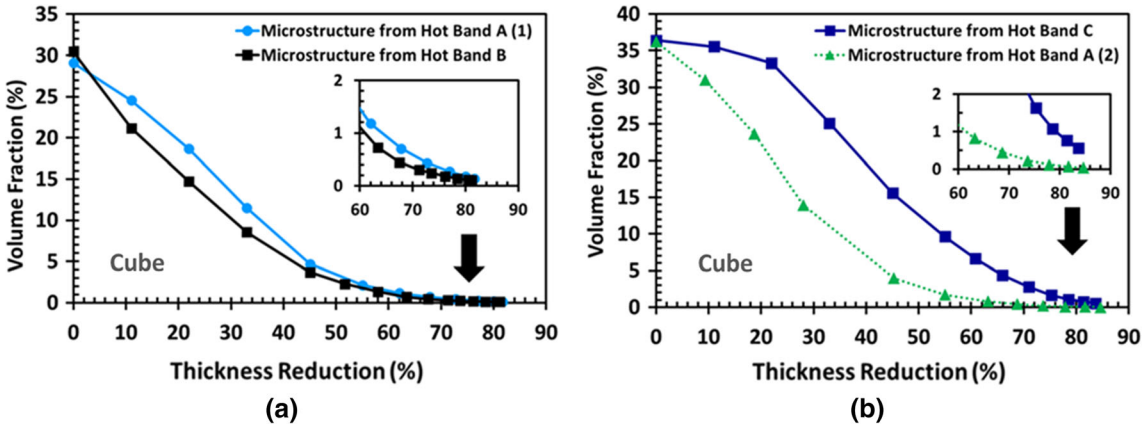

Fig. 10—Evolution of Cube volume fraction as function of thickness reduction extracted from crystal plasticity simulations. Comparison of Cube evolution for microstructures from hot band A and hot band B (*a*) and for microstructures from hot band A and hot band C (*b*).

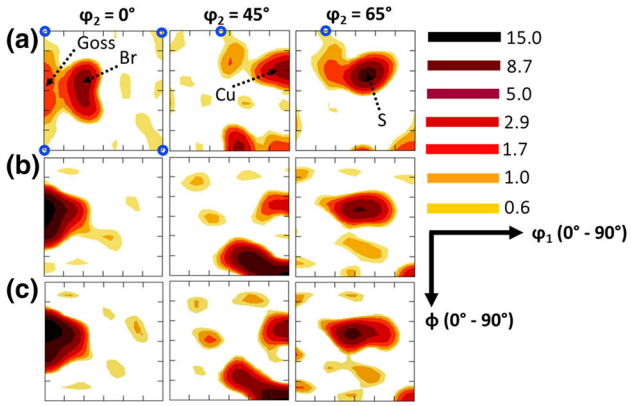

Fig. 11—Orientation distribution function (ODF) sections for φ_2 0, 45, 65 deg of: cold-rolled sample from hot band A (*a*) (ODF maximum intensity 13.8), crystal plasticity simulations of cold rolling on microstructures from hot band A (*b* and *c*) (ODF maximum intensity 25.6 and 24.0, respectively).

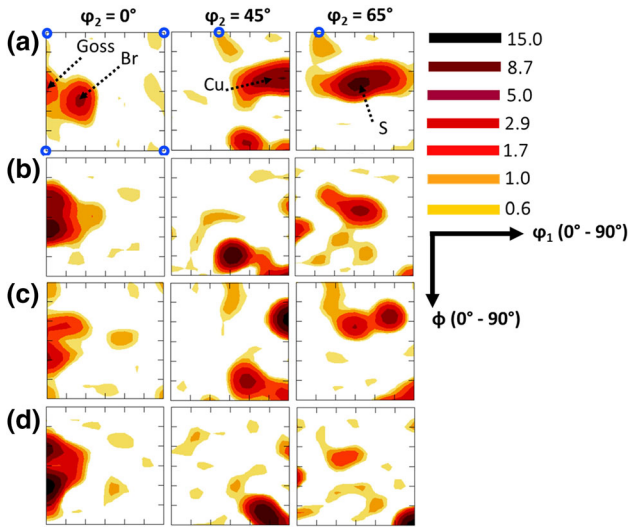

Fig. 12—Orientation distribution function (ODF) sections for φ_2 0, 45, 65 deg of: cold-rolled sample from hot band B (*a*) (maximum intensity 19.91) and from crystal plasticity simulation of cold rolling on microstructures from hot band B (*b*) (maximum intensity 31.0). ODF sections for φ_2 0, 45, 65 deg of cold-rolled sample from hot band C (*c*) (maximum intensity 17.5) and from crystal plasticity simulation of cold rolling on microstructures from hot band C (*d*) (maximum intensity 26.3).

locally. This tends to underestimate Brass in 2D RVEs,[3] while for a 3D RVE, the F_{RD-TD} is globally zero (as required by a plane strain compression load), but locally can be non-zero. Having F_{RD-TD} both globally and locally equal to zero brings to an overestimation of Goss,[3] which is known to be a stable orientation up to large strains.[28,50] The intensity of ODFs is higher for crystal plasticity simulations than for experiments because of the limited number of orientations available from the simulations. Moreover, the experimental ODFs in Figures 11 and 12 were plot considering the whole RD–ND section, while crystal plasticity simulation is limited to a small area.

E. *Cube Neighbors, Dislocation Density, and Particle Size Analyses*

From the previous results, it is not a difference in Cube volume fraction remaining in the microstructure at the end of cold rolling that can justify the different volume fractions of Cube in the recrystallized materials.

According to the literature,[31] two theories explain the origin of high Cube fraction at the end of recrystallization: the oriented nucleation and the oriented growth which can be both originated by high mobility grain boundaries where the relation between Cube and the neighbor is 40 deg ⟨111⟩. This orientation relation would be found between 20 deg ND rotated Cube ({001}⟨310⟩) and Copper,[51] while others mention that this orientation relation can be found between the Cube and the S texture component.[24] For aluminum, Hjelen *et al.*[51] have shown that Cube transition bands promoting Cube recrystallization can be formed inside or at interfaces to Copper orientation. Here, several high-resolution EBSD maps with 80 nm step size were obtained around Cube grains from all three cold-rolled microstructures. The cold-rolled specimen from hot band A (*i.e.*, without heat treatment between hot and cold rolling) has Cube grains which are very often surrounded by S and Copper orientations. Figures 13(a) through (d) shows IPFs along ND direction for several Cube bands found in the sample cold rolled from hot band A. The Cube/S, Cube/Copper, and Cube 20 deg ND rotated/Copper distributions are shown. In all regions, Cube is always in contact with S or Copper, and some regions show zones where Cube 20 deg ND rotated is in contact with Copper.

EBSD maps obtained from Cube grains in cold-rolled samples from hot bands B and C (Figures 14 and 15 respectively) show Cube grains not directly in contact with S or Copper but instead surrounded by random orientations. Zones extracted from these specimens have also several large precipitates (Al–Fe–Si precipitates up to 10 μm in length) which are close to Cube grains and seem to be fragmented during cold rolling. As discussed by Lücke and Engler,[8] large non-shearable particles (main size > 1 μm) weaken the overall texture creating zones with random orientations due to PSN causing a decrease of Cube fraction in recrystallized microstructures. According to Dons and Nes,[47] AlFeSi precipitates promote PSN and are responsible for texture randomization. The amounts of iron and silicon in the AA 6016 used for the present experiments justify the presence of AlFeSi particles.[47] Even though a pheno--power law was used for the simulations, the shear stresses can be translated into dislocation density using the Taylor equation [$\tau(t) = \tau_0 + \alpha G b\sqrt{\rho}$, with τ_0 as the initial shear strength, G the shear modulus of aluminum, b the Burger's vector, α a factor equal to 0.3 and ρ as dislocation density] and assuming an initial density of the hot bands of the order of 10^8 m^{-2}. In Figure 16, the dislocation density from crystal plasticity simulations was calculated and compared for all cold-rolled microstructures from hot band A, B, and C. The dislocation density distribution suggests that microstructures from hot band A have slightly higher

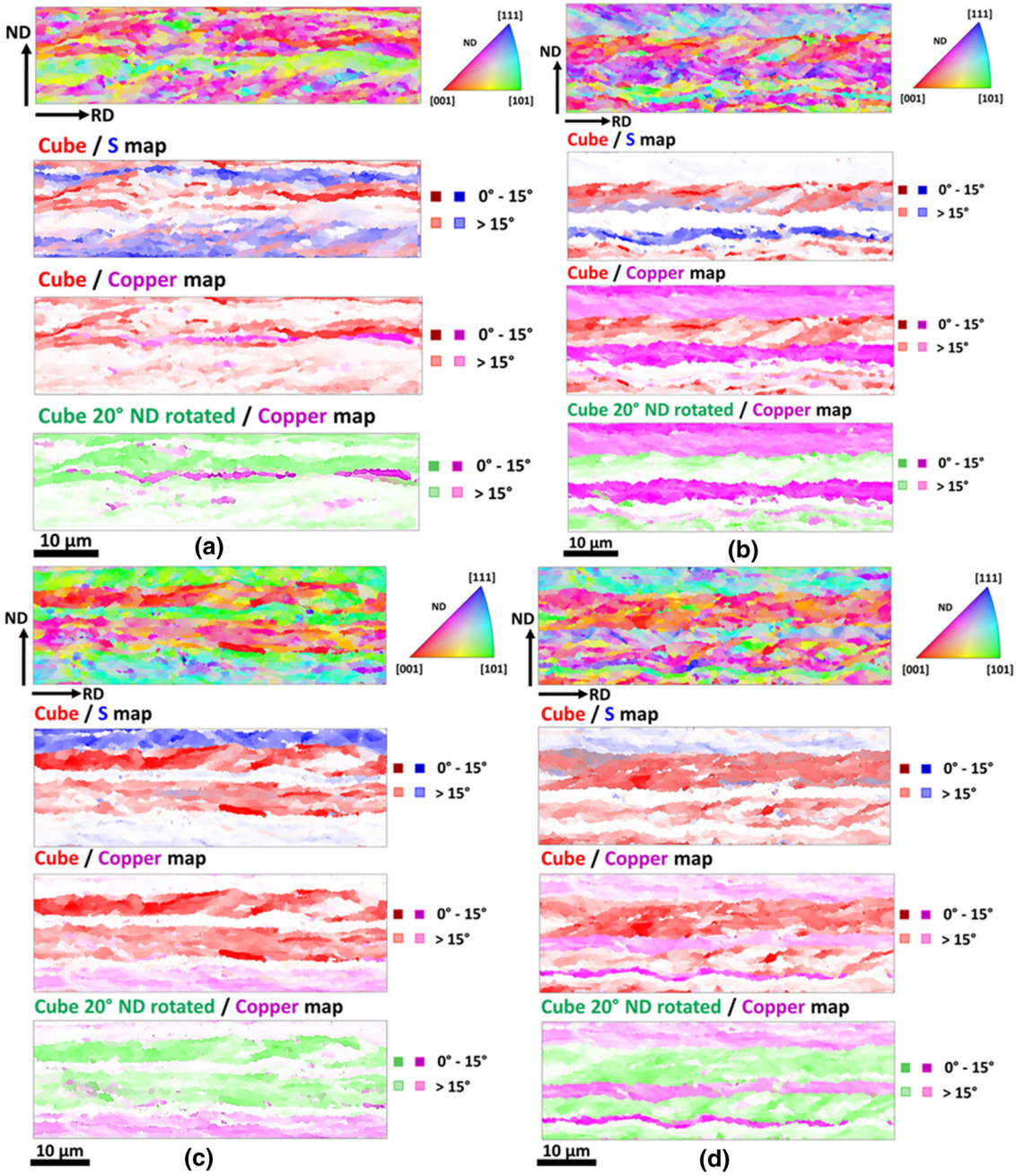

Fig. 13—IPF (ND) of several Cube bands inside the cold-rolled sample from hot band A (*a* through *d*). Cube/S, Cube/Copper, and Cube 20 deg ND rotated/Copper maps are provided for each EBSD map.

dislocation density than microstructures from hot bands B and C, but the difference is not significant and this confirms that at thickness reductions higher than 80 pct, the initial grain size of the hot band does not play a major role in texture and dislocation density evolution. This was confirmed by experiments on polycrystalline Copper where the stored deformation energy of fine and coarse microstructures was compared showing that after 70 pct of reduction, the values of stored energies are the same.[30] Another parameter analyzed to understand if a microstructure is prone to recrystallization is the kernel average misorientation (KAM). The KAM was extracted both from RD–ND sections from crystal plasticity simulations (Figures 17(a) and (b)) and from EBSD maps of the RD–ND section of the whole thickness of the specimen (Figures 17(c) and (d)). The KAM was calculated considering all points in a kernel up to a 3rd order neighbor in scans with the same step size. As shown in Figure 17, both in simulations and experimental EBSD maps, the KAM distribution and maximum peak is at larger angles for the microstructures obtained from cold rolling of hot band A. Thus, cold rolling from hot bands B and C will produce cold-rolled microstructures with lower KAM compared

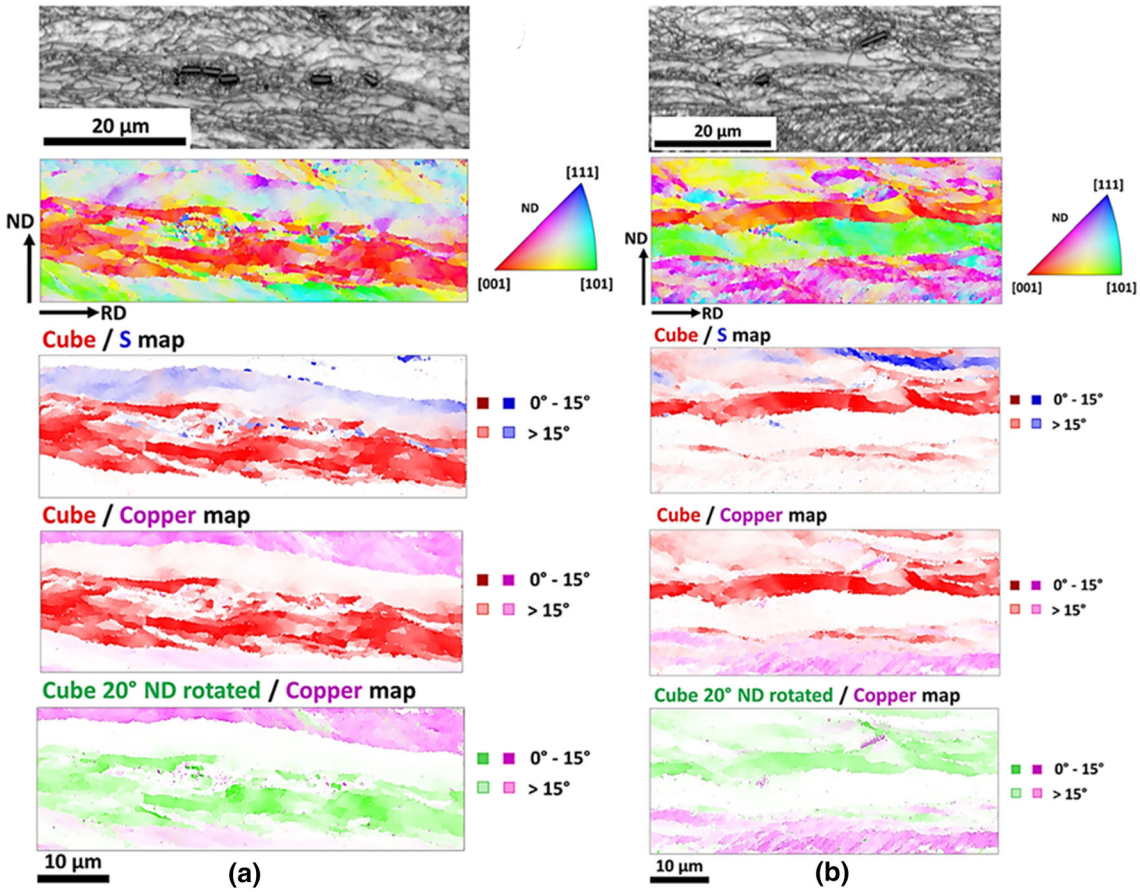

Fig. 14—IPF (ND) of Cube bands inside the cold-rolled sample from hot band B (*a*, *b*). Cube/S, Cube /Copper, and Cube 20 deg ND rotated/ Copper maps are provided for each EBSD map.

to hot bands without annealing. The lower KAM for specimens from hot bands B and C is another factor decreasing the probability of Cube recrystallization.

The distribution of precipitates dimension was analyzed in hot bands and in the corresponding cold-rolled specimens and their size distribution is plotted as function of the aspect ratio and of the ellipse angle (Figure 18). The majority of the particles are in the shape of rods and the ellipse angle is 0 deg if the precipitates are aligned with the rolling direction and it increases as they rotate away from this direction. Precipitates pertaining to magnesium and silicon as well as Fe/Mn-containing dispersoids are present; however, their size is too small ($< 0.25\ \mu m$) and they are not considered in the particle distribution analysis. Only precipitates with an area $> 0.22\ \mu m^2$ and a major length $> 0.6\ \mu m$ together with a bright appearance in the backscatter electron (BSE) images (originating mainly from Fe) are considered (see "Appendix", Figure A-IV). The average particle size in the hot bands is not significantly altered due to annealing (see the averaged sized particle displayed in purple in Figure 18). After cold rolling, the fragmentation is more pronounced in CR-A, while hot bands B and C maintain the same average particle size after cold rolling, based on the mean values of area and major length that are both about 50 pct smaller in CR-A than CR-B and CR-C. The finer and elongated grain size and thus the higher fraction of grain boundaries present in hot band A can be responsible for a more pronounced fragmentation of precipitates due to an increased probability of interaction between dislocations pile up at grain boundaries and precipitates. Moreover, the microstructure of hot band A was not annealed, thus its dislocation density should be higher than the dislocation density of hot band B and C before cold rolling. These two factors could increase the probability of dislocations interacting with precipitates causing more pronounced fragmentation in hot band A.

This precipitates distribution seems to confirm that PSN plays a more important role to texture evolution and randomization during recrystallization of rolled specimens from hot bands B and C than recrystallization of cold-rolled samples stemming from hot band A.

Figure 19 shows the 0, 45, and 65 deg sections of the ODF for hot bands A, B, and C and of samples cold rolled and SA. The texture of hot band A has a significant intensity of Cube, but also a fully developed β fiber texture with Brass, Copper, and S components, while hot bands B and C have high intensity for exact

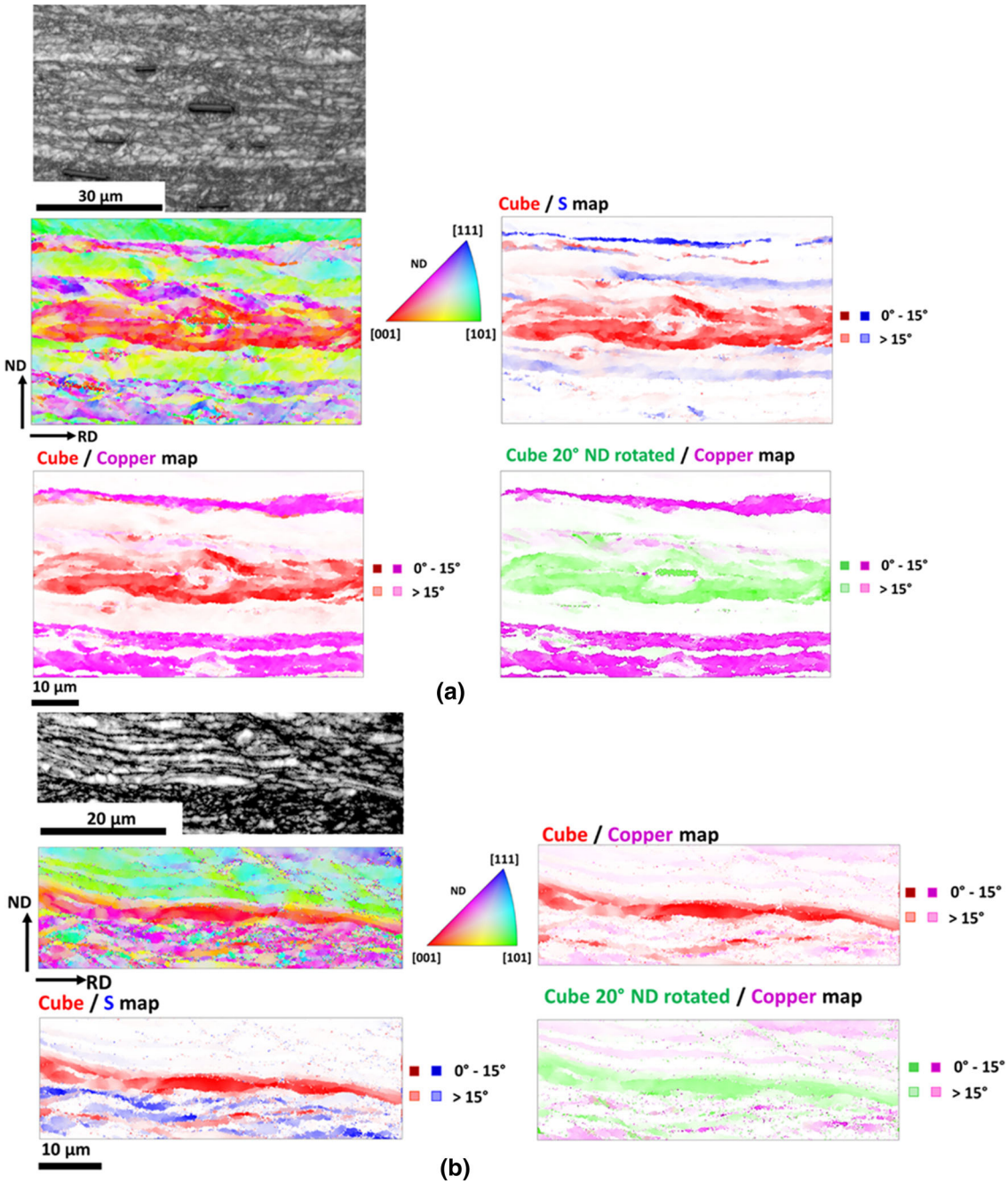

Fig. 15—IPF (ND) of Cube bands inside the cold-rolled sample from hot band C (*a*, *b*). Cube/S, Cube /Copper, and Cube 20 deg ND rotated/ Copper maps are provided for each EBSD map.

Cube and rotated Cube orientations, but the β fiber components are negligible (Figure 19(a)). The intensity of Cube texture after cold rolling and solution annealing is diminished for microstructures cold rolled from hot bands B and C while it increases for the microstructure from hot band A. The maximum ODF intensity for the specimen from hot band A is 28.0 and it is found at the exact Cube orientation, while for both specimens from hot bands B and C, the maximum intensity is lower than 7.0 and it is not found in correspondence to the exact Cube orientation. Moreover, the specimen from hot band A, after solution annealing, has Cube with RD scatter or exact Cube orientation, while samples from hot bands B and C have little Cube with exact orientation and show a scatter of Cube along ND direction. The influence of intermediate annealing during cold rolling was investigated by Engler[52] by applying a heat treatment at 56 pct or at 80 pct

thickness reduction on alloy AA 5182. The heat treatment was done at a temperature of 400 °C for 4 min in a salt bath. Annealing after a certain amount of cold rolling was effective in reducing the Cube texture[52]; however, the introduction of the heat treatment before the starting of the cold rolling reduces the Cube intensity even further. Intermediate annealing after more than 50 pct of cold rolling could reduce Cube intensity only of a factor 2,[52] while in the results presented in Figure 19, the maximum ODF intensity has been reduced of a factor 4 and its maximum is not found at the exact Cube orientation. In the work of Engler,[52] the introduction of the intermediate annealing after more than 50 pct of cold rolling should have diminished the rolling texture but also the dislocation density and both factors should have a positive effect in limiting the Cube intensity during the final recrystallization. However, it cannot be excluded that during intermediate annealing after more than 50 pct of cold rolling, the Cube grain size was increased causing a higher fraction of Cube left in the microstructure during the successive 30 pct of thickness reduction.[52] Moreover, PSN in AA 5182 was probably not as strong as in AA 6016.

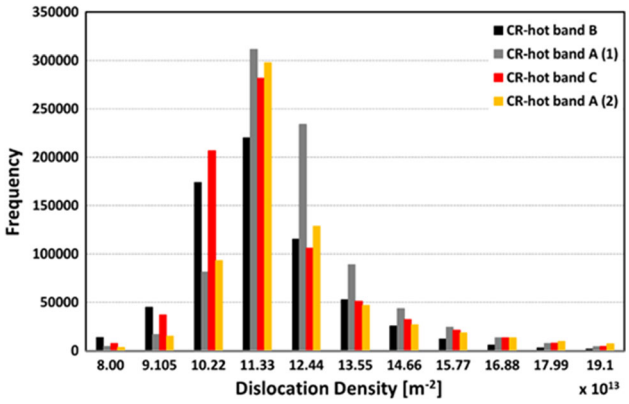

Fig. 16—Dislocation density calculated from crystal plasticity simulations for microstructures from hot bands A, B, and C. CR-hot band A (1) and CR-hot band A (2) refer to the cold-rolled microstructures obtained by simulations of two zones from hot band A.

The work presented here proves that the texture of the initial hot band has an influence on the texture found in the aluminum sheet after cold rolling and annealing. Previously, Dons and Nes[47] tried to investigate the influence of different initial hot band textures on the microstructure and texture obtained after cold rolling and recrystallization in Al–Fe–Si alloys. They started

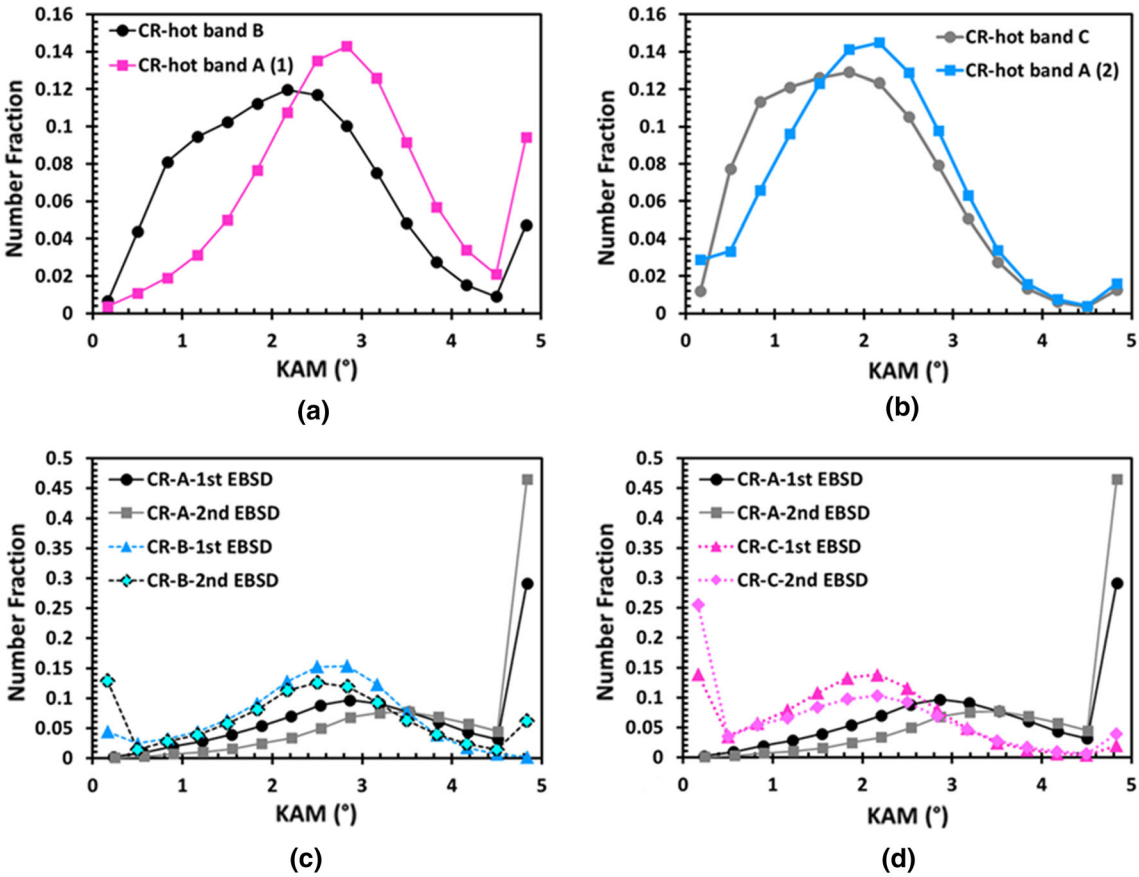

Fig. 17—Kernel average misorientation (KAM) extracted from crystal plasticity simulations for microstructures cold rolled from hot band A, B, and C (*a*, *b*). KAM extracted from EBSD maps of cold-rolled samples from hot bands A, B, and C (*c*) and (*d*). CR-hot band A (1) and CR-hot band A (2) refer to the cold-rolled microstructures obtained by simulations of two zones from hot band A.

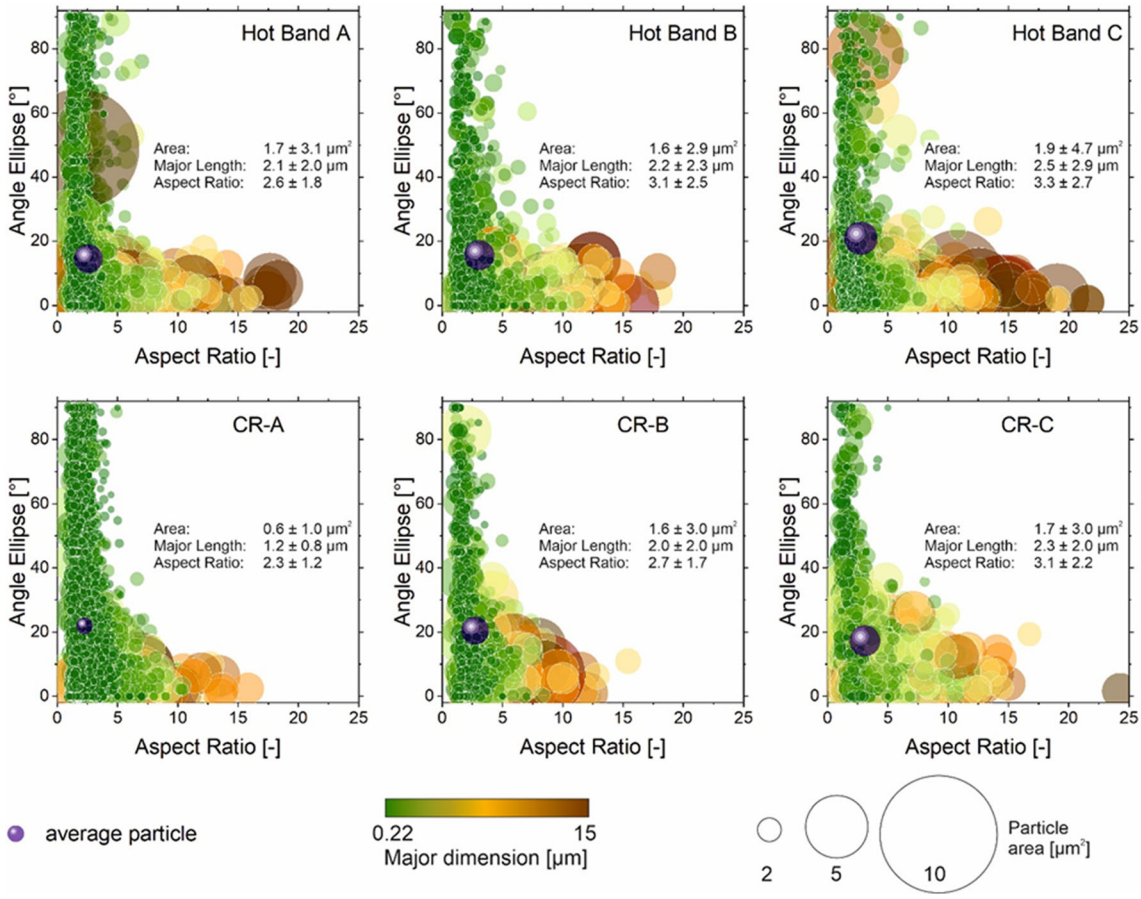

Fig. 18—Morphology of primary precipitates in specimens from hot bands A, B, and C and the corresponding cold-rolled samples A, B, and C. The bubbles diameter represents the particle´s area in (μm^2), the color represents its diameter. The ellipse angle on the *y*-axis represents a particle´s alignment with the rolling direction (0 deg deviation = major axis in RD) (Color figure online).

with a recrystallized hot band having strong Cube texture at the sheet center and random texture at the sheet surface, but after cold rolling and recrystallization, the Cube fraction was the same both at the center and at the surface.[47] It is true however, that their hot band was annealed at a temperature of 285 °C for 24 hours, while the recrystallization treatment after cold rolling was done at 400 °C for 3 min, so all temperatures are lower than the annealing temperatures applied in the present work. At low recrystallization temperatures, Cube nucleation is favored over other mechanisms (such as strain-induced boundary migration and PSN) and over nucleation of other orientations because of the fast Cube recovery.[44,53]

IV. CONCLUSIONS

The introduction of an intermediate heat treatment at the end of hot rolling and before cold rolling on AA 6016 results in a viable solution to reduce the volume fraction and intensity of Cube texture after solution annealing at the end of cold rolling. The intermediate annealing between hot and cold rolling changes the grain size in the hot band; however, this does not affect the Cube texture fraction during cold rolling for thickness reductions equal or higher than 80 pct. The dislocation density is expected to be similar in all cold-rolled specimens as a consequence of the high thickness reduction. Although the Cube fraction is similar in all cold-rolled samples, strong differences are found in Cube fraction after solution annealing because the initial grain size of the hot bands affects shape, thickness, and distribution of Cube in the cold-rolled microstructure.

For samples cold rolled from annealed hot bands, the lower intensity and fraction of Cube after solution annealing is attributed to the decrease of intensity of β fiber orientations. The removal or decrease of β fiber components lowers the probability of finding the remaining Cube grains surrounded by S or Copper. Moreover, Cube bands and their growth facilitating

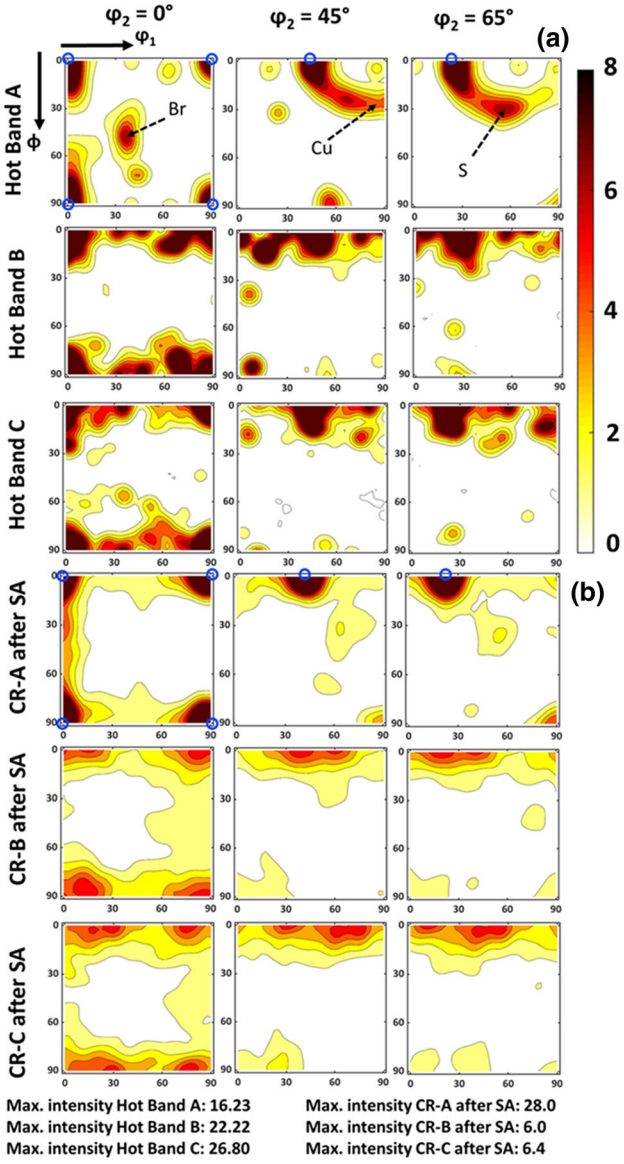

Fig. 19—ODF sections (φ_2 of 0, 45, and 65 deg) for hot bands A, B, and C (*a*) and of cold-rolled samples from different hot bands after solution annealing (*b*). The circles indicate position of exact Cube orientation. Position of Brass (Br), Copper (Cu), and S is indicated by arrows in the ODF plots of hot band A.

interfaces are further apart in the microstructures obtained from annealed hot bands. In addition, PSN seems to be favored in cold-rolled specimens from AA 6016 annealed hot bands and it contributes to texture randomization.

ACKNOWLEDGMENTS

The authors wish to express their sincere thanks to AMAG Rolling for providing the material and for the valuable discussions. This work was funded by the Christian Doppler Research Association within the framework of the Christian Doppler Laboratory for Advanced Aluminum Alloys. Financial support from the Austrian Federal Ministry for Digital and Economic Affairs, the National Foundation for Research, Technology and Development, and the Christian Doppler Research Association is gratefully acknowledged. The authors thank Monika Nellessen at Max-Planck Institut für Eisenforschung for her assistance on the EBSD experiments.

AUTHOR CONTRIBUTIONS

EC: Conceptualization, Methodology, Investigation, Formal analysis, Visualization, Writing-original draft, Writing-review and editing. IW: Investigation, Formal analysis, Visualization, Writing-review and editing. JG: Investigation, Writing-review and editing. GF: Investigation, Writing-review and editing. SP: Resources, Writing-review and editing, Supervision, Funding acquisition. FR: Resources, Writing-review and editing, Supervision, Funding acquisition.

CONFLICT OF INTEREST

The authors declare that they have no known competing financial interests or personal relationships that could have appeared to influence the work reported in this paper.

FUNDING

Open Access funding enabled and organized by Projekt DEAL.

OPEN ACCESS

APPENDIX: ADDITIONAL ELECTRON BACK SCATTERED DIFFRACTION MAPS AND BACK SCATTERED ELECTRON (BSE) IMAGES

See Figures A-I through A-IV.

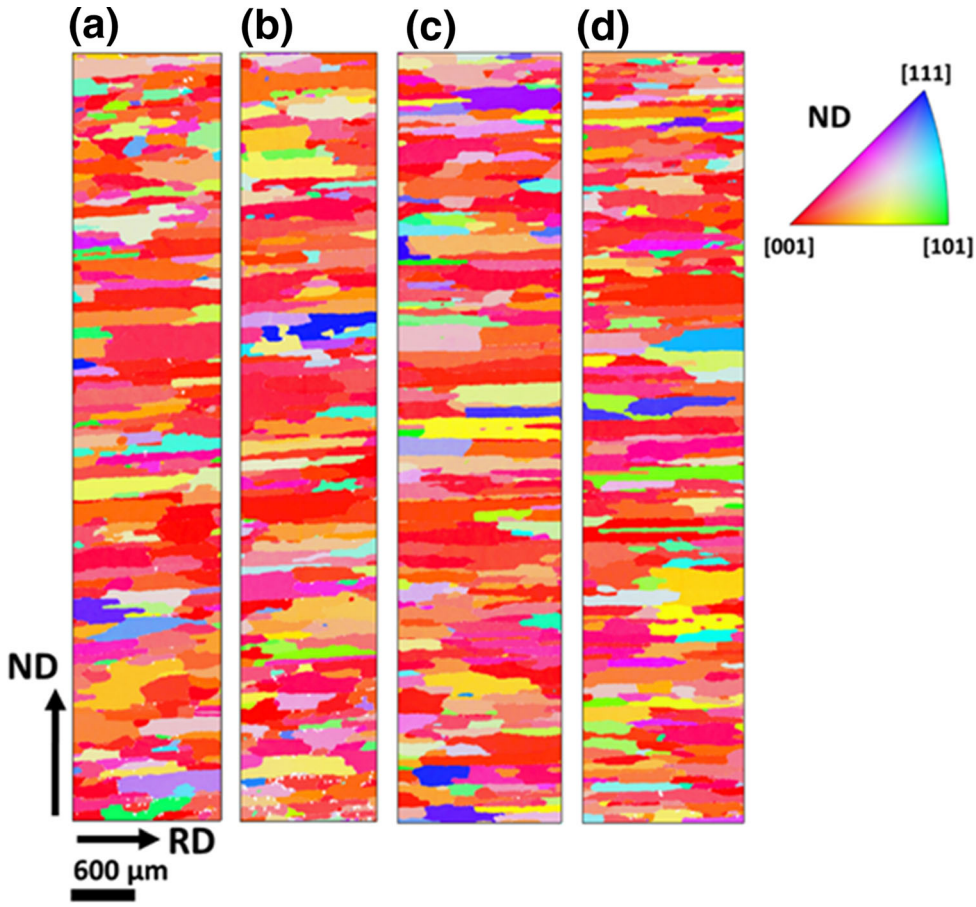

Fig. A-I—Inverse pole figures for normal direction (ND) for RD–ND section of hot band B (*a* and *b*) and for hot band C (*c* and *d*) (EBSD step size of 4 μm).

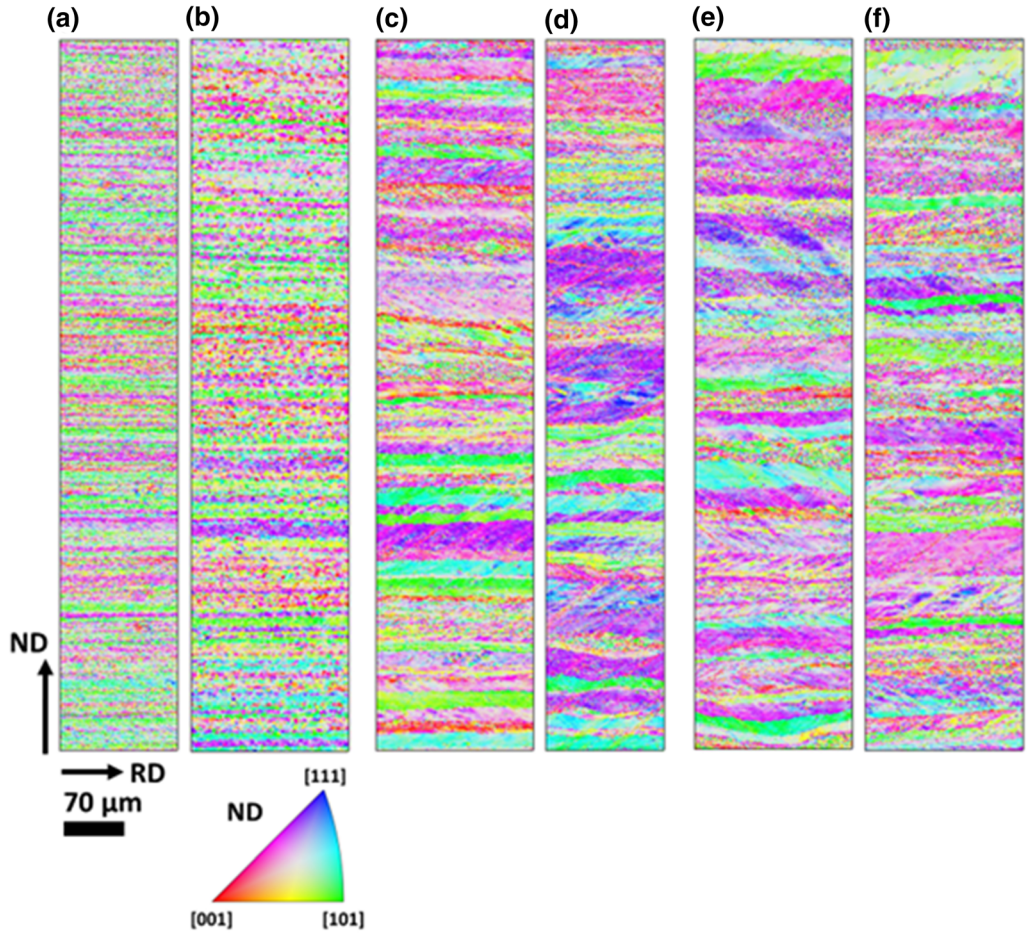

Fig. A-II—Inverse pole figures for normal direction (ND) for RD–ND sections of cold-rolled samples (CR) from hot band A (*a* and *b*), from hot band B (*c* and *d*) and from hot band C (*e* and *f*) (EBSD step size of 1.5 μm).

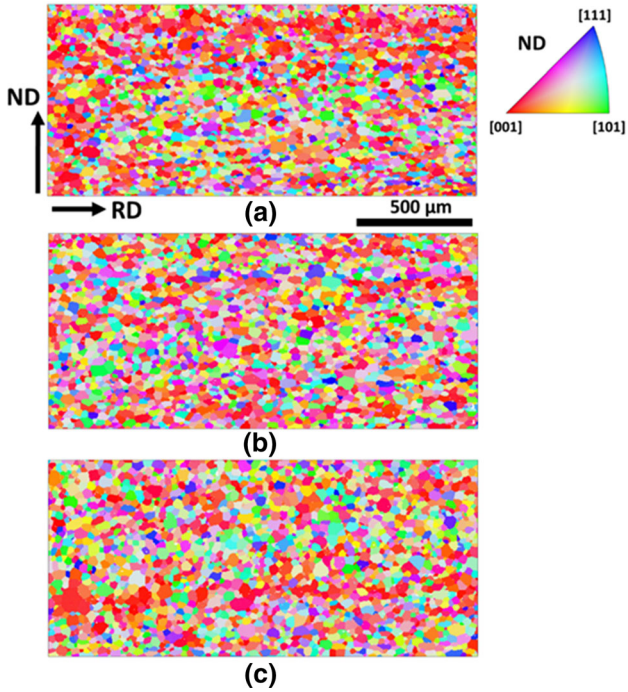

Fig. A-III—Inverse pole figures for normal direction (ND) for RD–ND sections of cold-rolled samples (CR) from hot band A (*a*), hot band B (*b*), and hot band C (*c*) after solution annealing (SA) (EBSD step size of 3 μm).

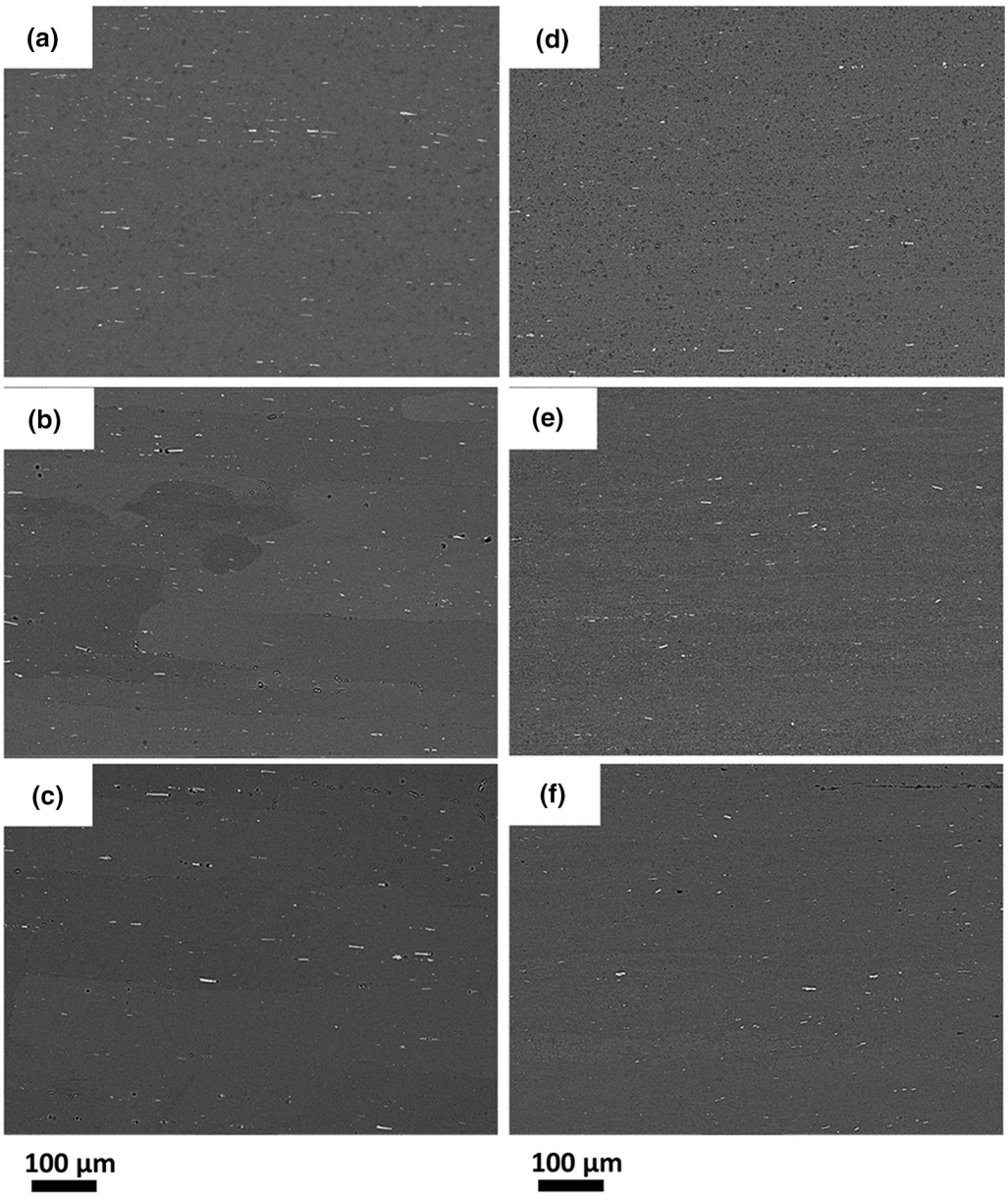

Fig. A-IV—Back scattered electron (BSE) images of hot bands A (*a*), B (*b*), and C (*c*) and the corresponding cold-rolled microstructures (*d* through *f*).

REFERENCES

1. O. Engler and J. Hirsch: *Mater. Sci. Eng. A*, 2002, vol. 336, pp. 249–62.
2. W.C. Liu, T. Zhai, and J.G. Morris: *Scripta Mater.*, 2004, vol. 51, pp. 83–88.
3. E. Cantergiani, G. Falkinger, S. Mitsche, M. Theissing, S. Klitschke, and F. Roters: *Metall. Mater. Trans. A*, 2022. https://doi.org/10.1007/s11661-022-06710-5.

4. J. Sidor, R.H. Petrov, and L. Kestens: *Comprehensive Materials Processing: Advanced Forming Technologies*, vol. 3, Elsevier, Amsterdam, 2014, pp. 447–98.
5. W. Truszkowski, J. Krol, and B. Major: *Metall. Trans. A*, 1982, vol. 13, pp. 665–69.
6. W. Truszkowski, J. Krol, and B. Major: *Metall. Trans. A*, 1980, vol. 11, pp. 749–58.
7. A.K. Vasudévan, M.A. Przystupa, and W.G. Fricke: *Mater. Sci. Eng. A*, 1996, vol. 208, pp. 172–80.
8. K. Lücke and O. Engler: *Mater. Sci. Technol.*, 1990, vol. 6, pp. 1113–30.
9. W. Wen, W.C. Liu, and J.G. Morris: *Mater. Sci. Eng. A*, 2004, vol. 380, pp. 191–207.
10. A. Albou, S. Raveendra, P. Karajagikar, I. Samajdar, C. Maurice, and J.H. Driver: *Scripta Mater.*, 2010, vol. 62, pp. 469–72.
11. J. Hirsch and T. Al-Samman: *Acta Mater.*, 2013, vol. 61, pp. 818–43.
12. O. Engler and J. Hirsch: *Mater. Sci. Forum*, 1996, vol. 217–222, pp. 479–86.
13. C.S. Lee, R.E. Smallman, and B.J. Duggan: *Scripta Metall. Mater.*, 1993, vol. 29, pp. 43–48.
14. I.L. Dillamore and H. Katoh: *Met. Sci.*, 1974, vol. 8, pp. 73–83.
15. I.L. Dillamore, P.L. Morris, C.J.E. Smith, and W.B. Hutchinson: *Proc. R. Soc. A*, 1972, vol. 329, pp. 405–20.
16. F. Basson and J.H. Driver: *Acta Mater.*, 2000, vol. 48, pp. 2101–15.
17. I. Samajdar and R.D. Doherty: *Acta Mater.*, 1998, vol. 46, pp. 3145–58.
18. O. Sukhopar and G. Gottstein: *Int. J. Mater. Res.*, 2016, vol. 107, pp. 979–87.
19. O. Engler and M.Y. Huh: *Mater. Sci. Eng. A*, 1999, vol. 271, pp. 371–81.
20. G. Falkinger, K. Regl, and S. Mitsche: *Mater. Sci. Technol. (UK)*, 2019, vol. 35, pp. 1081–87.
21. O.V. Mishin, B. Bay, and D. Juul Jensen: *Metall. Mater. Trans. A*, 2000, vol. 31A, pp. 1653–62.
22. O.V. Mishin, B. Bay, G. Winther, and D.J. Jensen: *Acta Mater.*, 2004, vol. 52, pp. 5761–70.
23. T. Kamijo, H. Adachihara, and H. Fukutomi: *Acta Metall.*, 1993, vol. 41, pp. 975–85.
24. S. Chakraborty, C.S. Patil, and S.R. Niezgoda: *Metall. Mater. Trans. A*, 2022, vol. 53A, pp. 503–22.
25. Y.M. Zhao, W.C. Liu, and J.G. Morris: *Mater. Sci. Technol.*, 2003, vol. 19, pp. 1379–85.
26. E. Aryshenskii, J. Hirsch, S. Konovalov, V. Aryshenskii, and A. Drits: *Metals (Basel)*, 2021. https://doi.org/10.3390/met11060865.
27. Q. Zhao, Z. Liu, and M.A. Wahab: *Mater. Charact.*, 2020, vol. 169, p. 110643.
28. H. Paul and J. Driver: *Microchim. Acta*, 2006, vol. 155, pp. 235–42.
29. B. Radhakrishnan and G. Sarma: *JOM*, 2004, vol. 56, pp. 55–62.
30. R.D. Doherty: *Met. Sci.*, 1974, vol. 8, pp. 132–42.
31. O. Engler, H.E. Vatne, and E. Nes: *Mater. Sci. Eng. A*, 1996, vol. 205, pp. 187–98.
32. E. Koken, J.D. Embury, T.R. Ramachandran, and T. Malis: *Scripta Mater.*, 1988, vol. 22, pp. 99–103.
33. Q. Zhao, K. Huang, Y. Li, and K. Marthinsen: *Metall. Mater. Trans. A*, 2016, vol. 47A, pp. 1378–88.
34. S. Tangen, K. Sjølstad, T. Furu, and E. Nes: *Metall. Mater. Trans. A*, 2010, vol. 41A, pp. 2970–83.
35. M.M. Miszczyk, H. Paul, J.H. Driver, and J. Poplewska: *Acta Mater.*, 2017, vol. 129, pp. 378–87.
36. M.M. Miszczyk and H. Paul: *IOP Conf. Ser. Mater. Sci. Eng.*, 2018, vol. 375, pp. 1–9.
37. P. Du, H. Sun, Z. Wang, Y. He, G. Sheng, J. Zhang, and W. Liu: *J. Mater. Res. Technol.*, 2022, vol. 19, pp. 2388–2401.
38. J. Grasserbauer, I. Weißensteiner, G. Falkinger, S. Mitsche, P.J. Uggowitzer, and S. Pogatscher: *Materials (Basel).*, 2020, vol. 13 (2), p. 469. https://doi.org/10.3390/ma13020469.
39. F. Roters, M. Diehl, P. Shanthraj, P. Eisenlohr, C. Reuber, S.L. Wong, T. Maiti, A. Ebrahimi, T. Hochrainer, H.O. Fabritius, S. Nikolov, M. Friák, N. Fujita, N. Grilli, K.G.F. Janssens, N. Jia, P.J.J. Kok, D. Ma, F. Meier, E. Werner, M. Stricker, D. Weygand, and D. Raabe: *Comput. Mater. Sci.*, 2019, vol. 158, pp. 420–78.
40. M.A. Groeber and M.A. Jackson: *Integr. Mater. Manuf. Innov.*, 2014, vol. 3, pp. 56–72.
41. K. Sedighiani, V. Shah, K. Traka, M. Diehl, F. Roters, J. Sietsma, and D. Raabe: *Int. J. Plast.*, 2021, vol. 146, p. 103078.
42. M. Kasemer, G. Falkinger, and F. Roters: *Model. Simul. Mater. Sci. Eng.*, 2020, vol. 28, p. 085005.
43. O. Engler: *Mater. Sci. Technol.*, 1996, vol. 12, pp. 859–72.
44. O. Engler: *Textures Microstruct.*, 1995, vol. 23, pp. 61–86.
45. O. Engler, P. Yang, and X.W. Kong: *Acta Mater.*, 1996, vol. 44, pp. 3349–69.
46. M. Sindel, G.D. Köhlhoff, K. Lücke, and B.J. Duggan: *Textures Microstruct.*, 1990, vol. 12, pp. 37–46.
47. A.L. Dons and E. Nes: *Mater. Sci. Technol. (UK)*, 1986, vol. 2, pp. 8–18.
48. A.A. Ridha and W.B. Hutchinson: *Acta Metall.*, 1982, vol. 30, pp. 1929–39.
49. Q. Liu, Z. Yao, A. Godfrey, and W. Liu: *J. Alloys Compd.*, 2009, vol. 482, pp. 264–71.
50. M. Ferry and F.J. Humphreys: *Acta Mater.*, 1996, vol. 44, pp. 1293–1308.
51. J. Hjelen, R. Orsund, and E. Nes: *Acta Metall. Mater.*, 1991, vol. 39, pp. 1377–1404.
52. O. Engler: *Model. Simul. Mater. Sci. Eng.*, 2003, vol. 11, pp. 863–82.
53. O. Sukhopar and G. Gottstein: *Mater. Sci. Forum*, 2014, vol. 794–796, pp. 1245–50.